Journal of Sol-Gel Science and Technology
https://doi.org/10.1007/s10971-024-06520-8

Advancing ZMF-spinel ferrites with Gd^{3+} doping: structural, magneto-optical enhancements, and superior gamma-ray shielding for high-tech applications

Huda F. Khalil[1] · Shams A. M. Issa[2] · Sherif G. Elsharkawy[3] · Roya Boudaghi Malidarreh[4] · Sara Gad[1] · Ali Badawi[5] · Fatma Fakhry[6] · Hesham M. H. Zakaly[4,7,8,9]

Received: 20 May 2024 / Accepted: 13 August 2024

Abstract

In this investigation, the incorporation of Gd^{3+} ions into ZMF-spinel ferrites through the citrate sol-gel auto-combustion method significantly modified their structural, magneto-optical, and gamma-ray attenuation properties. Doping levels were varied across samples labeled ZMF0 to ZMF4 with Gd3+ concentrations ranging from 0.000 to 0.100. Advanced characterization techniques such as XRD, SEM, TEM, FT-IR, Raman spectroscopy, and XPS, alongside UV-vis spectroscopy and VSM measurements, highlighted the profound impact of Gd^{3+} doping. Notably, the incorporation of Gd^{3+} led to nano-sized cubic structures with an optimized crystallite size of 19.82 nm in the ZMF4 sample, and a notable reduction in the band gap from 3.21 eV to 2.99 eV was observed, indicative of enhanced electronic properties. Magnetic analysis revealed a transition towards superparamagnetic behavior, with a decrease in coercivity and squareness ratios, suggesting applications in areas such as data storage and optical waveguides. Furthermore, the study leveraged FLUKA Monte Carlo simulations to assess the gamma-ray shielding efficiency of these materials. It was found that increasing Gd^{3+} concentration or sample thickness markedly improved radiation attenuation, highlighting the material's enhanced shielding capabilities against a range of photon energies. The most significant findings included the optimized sample (ZMF4) displaying superior magneto-optical characteristics and outstanding gamma-ray shielding performance, especially at higher Gd^{3+} levels. This investigation underlines the critical role of Gd3+ doping in advancing the functional properties of ZMF-spinel ferrites for technological and radiation protection applications, showcasing the potential of tailored nanomaterials in addressing complex challenges in material science.

✉ Hesham M. H. Zakaly
h.m.zakaly@gmail.com

[1] Electronic Materials Department, Advanced Technology and New Material Institute (ATNMI), City of Scientific Research and Technological Applications (SRTA- City), Alexandria, Egypt

[2] Physics Department, Faculty of Science, University of Tabuk, Tabuk 47512, Saudi Arabia

[3] Basic and Applied Sciences, College of Engineering and Technology, AASTMT, Alexandria, Egypt

[4] Institute of Physics and Technology, Ural Federal University, Yekaterinburg 620002, Russia

[5] Department of Physics, University College of Turabah, Taif University, P.O. Box 11099, Taif 21944, Saudi Arabia

[6] Physics Department, Faculty of Science, Tanta University, Tanta, Egypt

[7] Istinye University, Faculty of Engineering and Natural Sciences, Computer Engineering Department, Istanbul 34396, Turkey

[8] Physics Department, Faculty of Science, Al-Azhar University, Assiut Branch, Assiut 71524, Egypt

[9] Department of Physics and Technical Sciences, Western Caspian University, Baku, Azerbaijan

Published online: 18 September 2024

Graphical Abstract

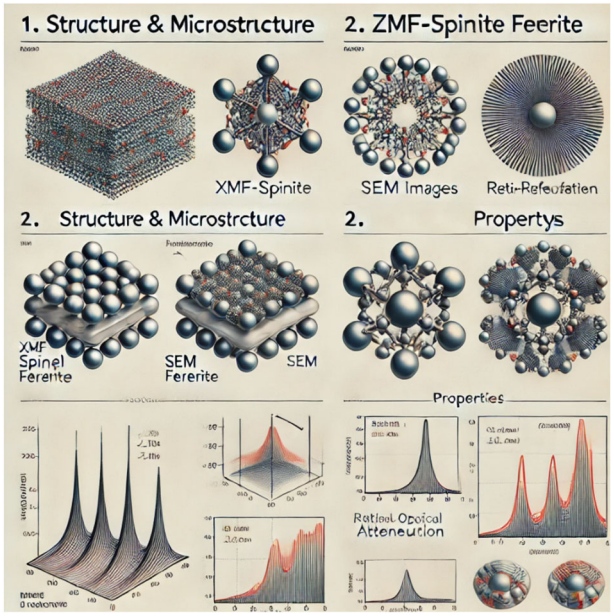

Keywords Spinel-ferrite · Magneto-optical properties · Rare earth Gd^{3+} ions · Superparamagnetic · Attenuation properties · Monte Carlo simulations

Highlights

- Gd^{3+} ion doping in ZMF-spinel ferrites reduced crystallite sizes to an optimal 19.82 nm, significantly enhancing their magneto-optical properties.
- Spectral analysis showed a noticeable blue shift in band edge absorption, with optical band gaps narrowing from 3.21 eV to 2.99 eV, indicating improved electronic properties.
- Magnetic assessments revealed a transition to soft magnetic behavior and identified superparamagnetic regions, broadening potential technological applications.
- FLUKA Monte Carlo simulations demonstrated that increased Gd^{3+} concentration and sample thickness significantly boost the material's gamma-ray shielding efficiency.
- The study's comprehensive analysis establishes ZMF-spinel ferrites doped with Gd^{3+} ions as promising candidates for advanced applications, including radiation protection and energy systems.

1 Introduction

Great interests are devoted to spinel ferrite materials (SFs), particularly with the commencement of the second millennium. Chemically formulated, MFe_2O_4 is a sub-class from the spinel structures which displayed quite remarkable superparamagnetic, electrical, and optical characteristics reflecting their unique composition [1–5]. Reducing the crystalline size in the nanoscale region plays a key role in enhancing the structural, magnetic, electronic, and optical properties of SFs [6]. The MFe_2O_4 classification commonly relies upon the location of M^{2+} cations relative to Fe^{3+} ones in tetrahedral and/or octahedral sites [7]. While M^{2+} cations are tetrahedral and Fe^{3+} cations are octahedral, normal spinels are obtained; meanwhile, M^{2+} cations are octahedral and Fe^{3+} cations are octahedral/tetrahedral, inverse spinels show up, and for random distribution [8] of M^{2+} and Fe^{3+} cations, complex spinels are found. Concurrently, metal cations' locations are dependent upon their affinity and consequently the stabilization energy, their ionic radii, the synthesis technique that controls the morphology of the resultant specimen, and the reaction conditions. Many [9] Ni^{2+} [10], Co^{2+} [11], Zn^{2+} [12], Mn^{2+} metal-based SFs have been investigated revealing amazing magnetic, electric and optical properties that are highly appropriate for different critical industries. Many researchers have synthesized and characterized different spinel ferrite structures such as MFe_2O_4 (M=Co [13], Cu [14], Mn [15], and Zn [16]). As a consequence of their ultimate resistivity and Curie temperature, SFs are interesting magnetic materials with a wide

range of technological applications and environmental stability. It is essential to adopt the proper crystalline characteristics as well as the proper choice of synthesis routine that will define the crystal lattice structure and its chemical composition, which would eventually produce quite enhanced properties for the new structure. Different techniques such as the sol-gel [17], co-precipitations [18], hydrothermal [19], mechanical method [20], facile sol-gel approach [21], micro-emulsion method [22], and thermal decomposition [23] method have been applied.

Radiation protection is paramount across various sectors such as nuclear energy, diagnostic radiology, and aerospace missions, given the detrimental health impacts linked to ionizing radiation exposure, including acute radiation syndrome and carcinogenesis [24, 25]. In the quest for superior radiation shielding solutions, Gd^{3+} doped $Zn0.5Mg0.5Fe_2O_4$ spinel ferrite nanoparticles have garnered significant interest for their potential in mitigating ionizing radiation risks. These nanoparticles, enhanced with rare earth Gd^{3+} ions, exhibit exceptional magneto-crystalline anisotropy and magnetic characteristics, positioning them as a promising material for effective radiation attenuation [26–28]. Gd^{3+} doping can modify the properties of $Zn_{0.5}Mg_{0.5}Fe_2O_4$ spinel ferrite for specific applications. Its large ionic radius allows it to substitute for Fe^{3+} ions without distortion. Although not magnetic, Gd^{3+} can influence magnetic interactions between Fe^{3+} ions. It can introduce additional functionalities like magnetostrictive or magneto-optical properties. Gd^{3+} doping affects the lattice parameter, crystallinity, saturation magnetization, coercivity, and band gap of the ferrite. The impact depends on the concentration and synthesis method used. Doping levels should be controlled to achieve desired properties without introducing secondary phases or degrading the material's performance. The inclusion of Gd^{3+} ions notably advances the gamma-ray shielding capabilities of $Zn_{0.5}Mg_{0.5}Fe_2O_4$ spinel ferrites, offering a path to refine and optimize these materials for critical radiation protection roles. Nanomagnetic materials, like Gd^{3+} doped $Zn_{0.5}Mg_{0.5}Fe_2O_4$, are at the forefront of research for radiation shielding due to their distinctive properties and adaptability, indicating a significant step forward in the development of advanced functional composites for safeguarding against ionizing radiation hazards [29–31].

Throughout this work, the $Zn_{0.5}Mg_{0.5}Fe_2O_4$ spinel ferrite (ZMF) composite was prepared by the citrate sol-gel auto-combustion method. The structure and its crystalline properties have been examined by using the XRD technique. The surface morphology was obtained by scanning electron microscopy, SEM. HR-TEM analysis was also performed. Fourier transform infrared, FT-IR, spectra were also obtained. RAMAN spectroscopy was adopted to study the internal structure. The X-ray photoelectron, XPS, investigated the binding energy. Also, the structures' absorption spectra were examined using a UV Spectrophotometer over the range of 340–500 nm. The magnetic properties were investigated using the VSM technique and the dM/dH was calculated. The novelty of this work is conducted throughout the doping of ZMF-spinel ferrite structure by the rare earth element Gd^{3+} ions at concentration ratios $x = 0.025$, 0.050, 0.075, and 0.100, respectively. The substitution of Gd^{3+} ions could strongly evolve further enhanced magneto-optical structure for SFs materials as the net magnetic moment of the rare earth Gd^{3+} ions, 7.94 μB [32], is larger than its corresponding of other rare-earth cations such as Lu^{3+} (0 μB) [33], Nd^{3+} (3.855 μB) [34], Yb^{3+} (4.63 μB) [35], and Pr^{3+} (3.4 μB) [36].

This study looks into what happens when Gd^{3+} ions are added to $Zn_{0.5}Mg_{0.5}Fe_2O_4$ spinel ferrite nanoparticles. It focuses on their structure, magneto-optical properties, and ability to block gamma rays. The novelty is that adding Gd^{3+} to the ZMF4 sample created nano-sized cubic structures with an ideal crystallite size of 19.82 nm. This meant that the electronic properties were better. Magnetic analysis revealed a transition towards superparamagnetic behavior, suggesting potential applications in data storage and optical waveguides. The study also showed that increasing Gd^{3+} concentration or sample thickness significantly improved radiation attenuation, highlighting the material's enhanced shielding capabilities against various photon energies. A lot of different advanced techniques were used by the authors, such as XRD, SEM, TEM, FT-IR, Raman spectroscopy, XPS, UV-vis spectroscopy, and VSM measurements, to get a full picture of the shielding properties. We chose the citrate sol-gel auto-combustion method for its precise control of composition and microstructure, which enables the fabrication of nanostructured materials with improved homogeneity and purity. The citrate sol-gel auto-combustion method, used in this study, produces highly homogeneous and fine powders with controlled stoichiometry and particle size. However, it faces challenges in precise control of combustion conditions, which can affect product consistency. The method's scalability for industrial applications is also a concern due to difficulties in maintaining uniform heating and reaction conditions. Future work should focus on optimizing combustion parameters, exploring alternative synthesis techniques, and investigating the long-term stability and performance of Gd^{3+}-doped $Zn_{0.5}Mg_{0.5}Fe_2O_4$ spinel ferrites in practical applications to fully understand their potential and limitations. This work provides a promising path towards the development of advanced functional materials for high-tech applications and radiation protection. Many potential applications could be considered for such enhanced superparamagnetic ZMF-spinel ferrite like Biomedicine [37], Magnetic Resonance Imaging (MRI)

[38], Environmental Remediation [39], Data Storage [40], and Energy Harvesting [41].

2 Experimental procedure

ZMF-spinel ferrite composite was successfully prepared by the citrate sol-gel auto-combustion technique. Aqueous solutions of $Zn(NO_3)_2.6H_2O$, $Mg(NO_3)_2.6H_2O$ $Gd(NO_3)_3.6H_2O$, and $Fe(NO_3)_3.9H_2O$ were dissolved in deionized water under stirring. Citric acid was weighed as 1:1 (g/mol) molar ratio then dissolved in deionized water under stirring with mild heating. All salts and Citric acid were mixed with continuous, uniform stirring at a 400 r/min rate for 1 h and 80 °C to prepare a homogeneous solution. The gel form was obtained when drops of NH_4OH solution were added to the homogeneous solution and then heated at 110 °C for gel combustion while the PH was controlled at around 10. After that, the gel was kept at 110 °C until burnt, and the gray ashes were obtained. These ashes were calcinated at 600 °C for 4 h to obtain $Zn_{0.5}Mg_{0.5}Fe_2O_4$ samples. Five samples at different Gd^{3+} concentrations; x = 0.000, 0.025, 0.050, 0.075, and 0.100, respectively were formed and were denoted as ZMF0, ZMF1, ZMF2, ZMF3 and ZMF4.

3 Samples characterization

Crystallinity and phase structure results of the synthesized SFs were obtained using X-ray diffraction analysis, XRD, Maxima.7000, Shimadzu. The test was performed with the aid of Cu-Kα radiation at wavelength of λ = 1.5418 Å and diffraction angles, 2θ, between 20°–70°. The surface morphology is captured and magnified by scanning electron microscopy, SEM; JEOL, the working conditions include 15 kV high voltage, 5.5 mm distance, 5 nm spot size, and 3000× magnification power. Also, Transmission Electron Microscopy (HR-TEM) is used to study the internal structure and morphology of the ZMF-spinel ferrite samples at very High Resolution, JEOL JEM-2100Plus. The FT-IR (Fourier Transform Infrared) module manufactured by Shimadzu, was used to acquire the infrared spectra. The spectra were collected over the wavenumber range of 250–4000 cm^{-1}. RAMAN spectroscopy was also used to study the internal structure in the range from 25 to 2000 cm^{-1}, Horiba Jobin Yvon LabRAM HR. The binding energy was investigated by X-ray Photoelectron Spectroscopy, XPS, Kratos AXIS Ultra DLD. The absorption spectra of ZMF-spienel ferrites were examined over 340–500 nm using UV/vis/NIR-spectrometer V-570, Jasco Inc. Finally, the magnetic properties were investigated with the aid of Vibrating Sample Magneto, VSM -Lakeshore 7400.

4 Results and discussions

4.1 XRD analysis

The results obtained by the XRD for all ZMF-spinel ferrite samples confirmed the formation of cubic spinel structures according to card number JCPDS #82-1049 [42], Fig. 1a. The preferred oriented peaks at angle 2θ were 29.64°, 34.14°, 34.56°, 54.52°, 60.85°, 65.91° and 67.03° corresponding to the miller indices as (220), (113), (400), (412), (511), (404) and (421) respectively. For more details, Fig. 1b, c represent $25 \le 2\theta^o \ge 40$ and $50 \le 2\theta^o \ge 65$, respectively, where the vertical dashed lines on each graph show clearly the deviation of the doped samples' peaks, towards positive x-axis direction. This behavior explains the diffusion of the Gd^{3+} ions through the structure. The lattice parameters a=b=c (Å) and the crystallite size D (nm) were determined using Scherrer's equation [43]:

$$D = \frac{k\lambda}{\beta \cos\theta} \tag{1}$$

$$d_{hkl} = \frac{a}{\sqrt{h^2 + k^2 + l^2}} \tag{2}$$

Where D is the crystallite size (nm), β is the full width at half maximum, θ is the Bragg's angle, and d is the interplanar distance of the crystal planes. Table 1 shows the Lattice parameter a (Å), crystallite size D (nm), volume V ($Å^3$), X-ray density (ρ_x) and Lattice strain (ε) for ZMF-spinel ferrite samples. Figure 1d shows a remarkable increase in the lattice parameter, a (Å), at ZMF1 (x = 0.025) with about 0.01 Å while decreasing for the rest of the concentration ratios. On the other side, the crystallite size D (nm) was found to decrease ≈ 2.11 nm for all ZMF-spinel ferrite samples. The Retiveld XRD refinement for all ZMF-spinel ferrite samples was fulfilled using FullProf software, Fig. 2. Among all structures, ZMF4 sample is claimed to be the optimized one since it possesses smallest crystallite size, 19.82 nm. Concluding that the Gd^{3+} doping mechanism has primarily enhanced the ZMF-spinel ferrite's structure would probably modify the other magneto-optical properties of the composite as will be seen in the next sections. The absorption bands observed in our study are indicative of the presence of certain crystalline phases within the material. These bands correspond to specific vibrational modes associated with the crystalline structure of the material. In the case of spinel structures, the characteristic absorption bands can be directly correlated to the distinct atomic arrangements and bonding within the crystal lattice. For example, the bands around 400 cm^{-1} and 650 cm^{-1} are typically associated with the stretching and bending vibrations of the M-O bonds (where M represents the metal ions) in spinel oxides. These bands serve as fingerprints for the spinel structure, confirming the

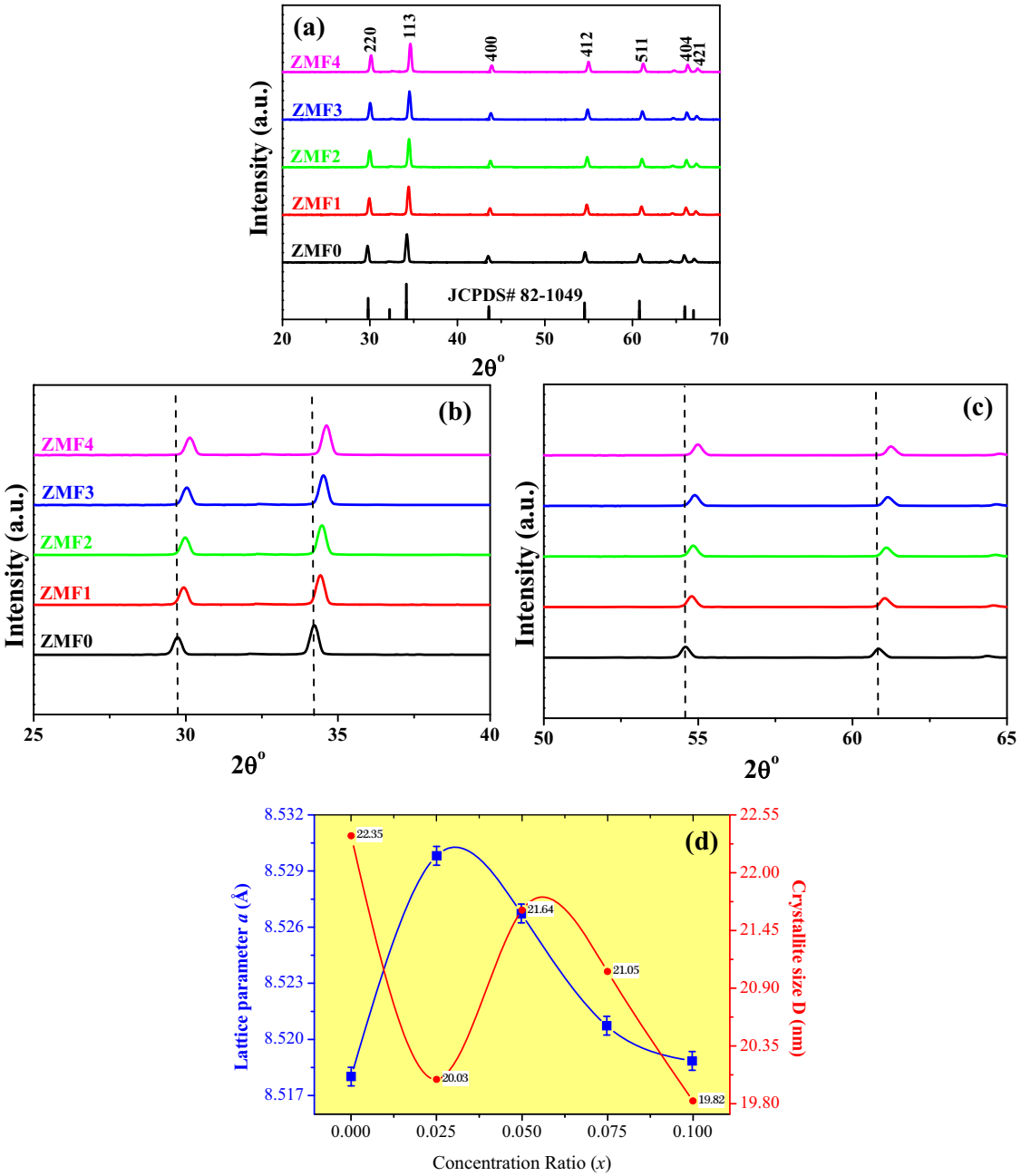

Fig. 1 XRD for (**a**) All ZMF-spinel ferrite samples ZMF0, ZMF1, ZMF2, ZMF3 and ZMF4, (**b**) $25 \leq 2\theta^{o} \geq 40$, (**c**) $50 \leq 2\theta^{o} \geq 65$, and (**d**) lattice parameter *a* (Å) and crystallite size D (nm)

Table 1 Lattice parameter *a* (Å), crystallite size D (nm), volume V (Å^3), X-ray density (ρ_x) and Lattice strain (ε) for ZMF-spinel ferrite samples

Samples	Lattice parameter *a* (Å)	D (nm)	V (Å^3)	ρ_x (g.cm^{-3})	Lattice Strain ε (%)
ZMF0	8.5180	22.35	618.03	4.741	0.00029
ZMF1	8.5298	20.03	620.61	4.773	0.00027
ZMF2	8.5267	21.64	619.93	4.833	0.00026
ZMF3	8.5207	21.05	618.62	4.898	0.00029
ZMF4	8.5188	19.82	618.21	4.959	0.00031

successful crystallization into this phase. The agreement between the absorption bands and the XRD data further supports the crystallization into the spinel structure. The absorption bands not only confirm the phase but also give insights into the purity and quality of the crystalline structure. The TEM and SAED analyses complement these findings by providing visual confirmation of the crystalline phases, showing clear lattice fringes and diffraction patterns consistent with spinel structures as we will see in the next section.

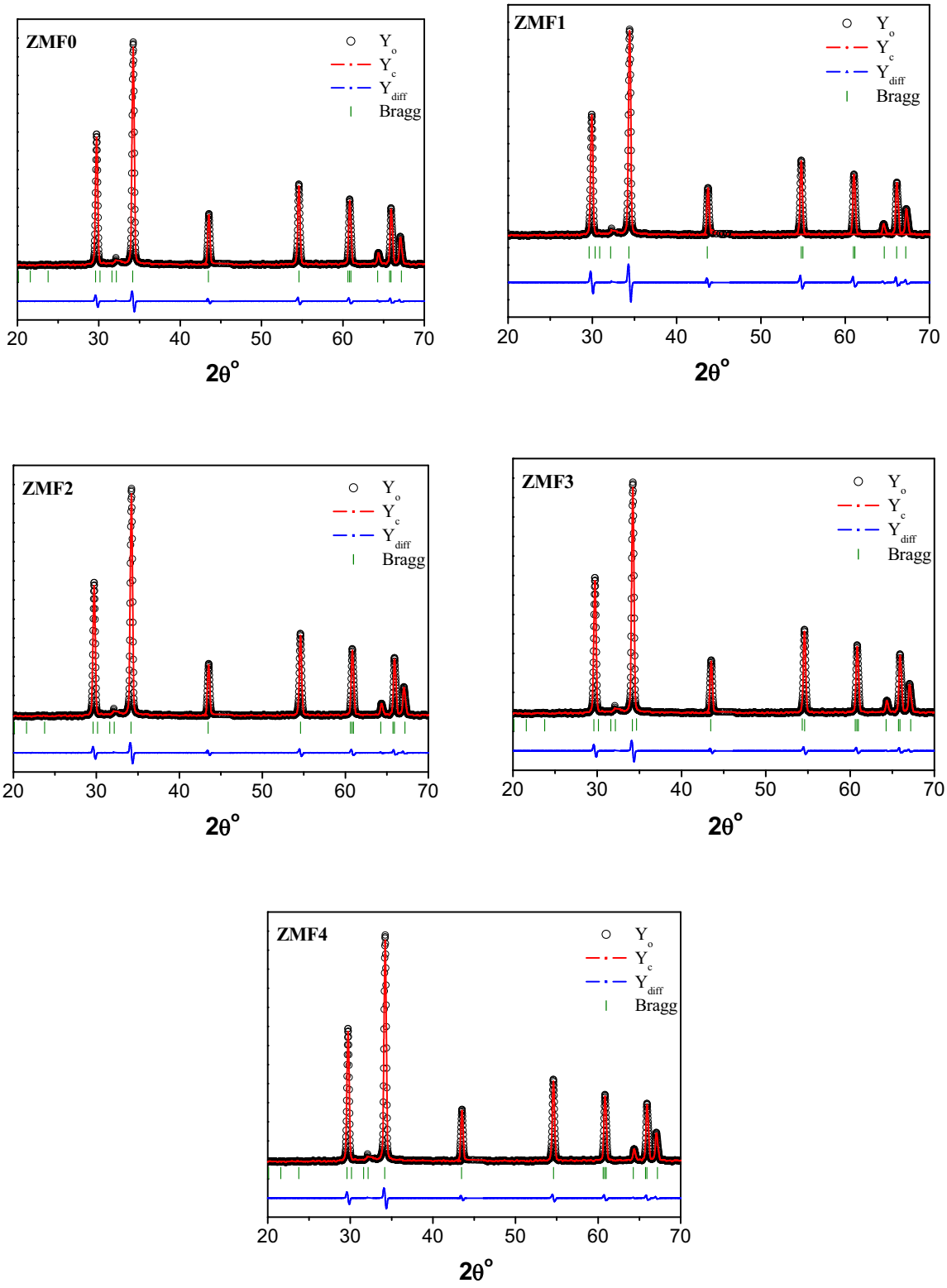

Fig. 2 Retiveld Refinement XRD for all ZMF-spinel ferrite samples ZMF0, ZMF1, ZMF2, ZMF3 and ZMF4

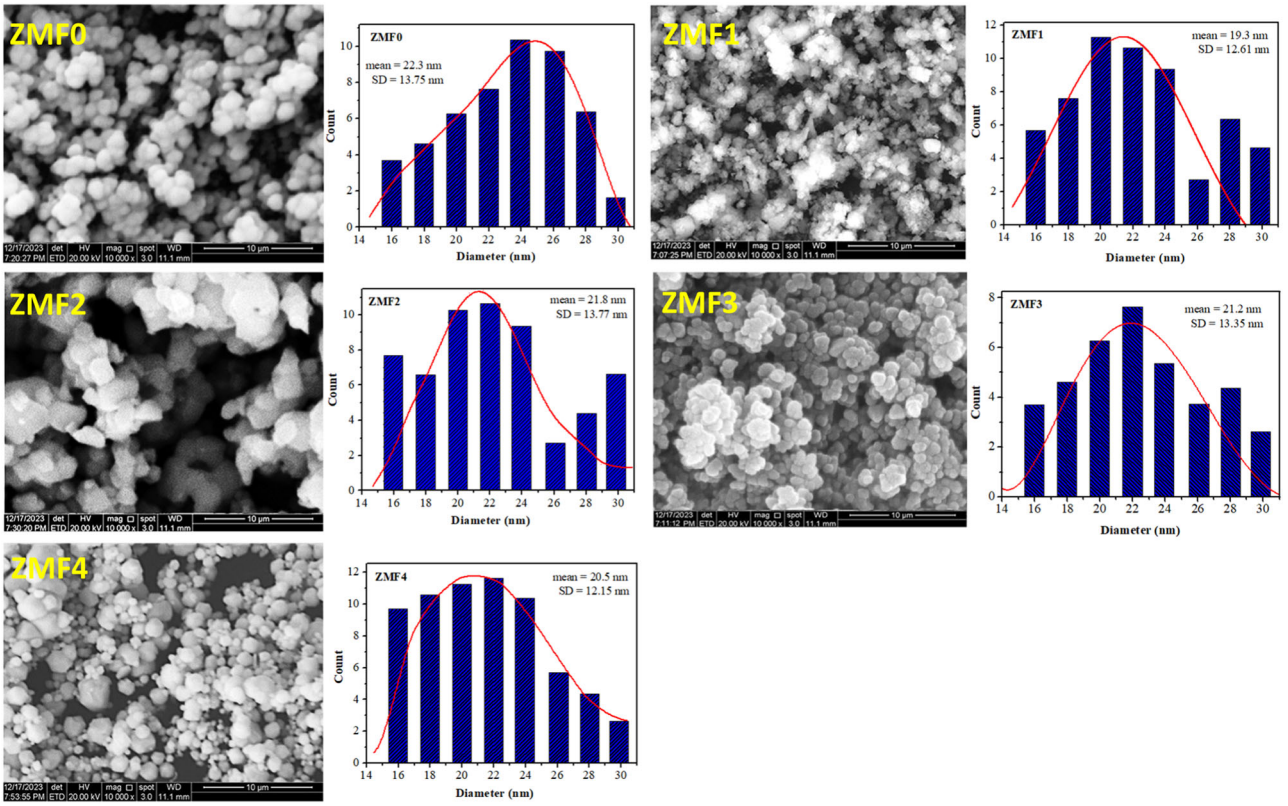

Fig. 3 SEM and particle size distribution images of ZMF-spinel ferrite samples

4.2 Morphology

4.2.1 Scanning electron microscopy (SEM) and particle size

The surface morphology and the particle size of the ZMF-spinel ferrite samples were examined using Scanning Electron Microscopy, SEM, Fig. 3. The SEM images showed the particles' enhancement [44] into spherical-like shape as the Gd^{3+} ions doping ratio was increased. This enhancement will be explained later in more details in the FT-IR and XPS analysis. Such results show that the optimized combination was obtained for the doped Gd^{3+} ZMF4 sample. Moreover, the average particles' diameters were diminishing from 22.3 to 20.5 nm reflecting the presence of the Nano-sized scale for all samples. These results are in consistent with that obtained for the crystallite size determined from XRD.

4.2.2 HR –TEM and SAED analysis

Figure 4 illustrates the HR-TEM, and SAED micrographs of ZMF-spinel nanoferrites for the pure ZMF0 and the optimized ZMF4 samples. The HR-TEM micrographs have proven the particles' nano-sized aggregated cubic structure. Such accumulated structure may be customized as a result of larger surface area and magnetic dipole interaction of the constituent ZMF-nanoparticles which increasing with increasing Gd^{3+} dopant ions [45]. Additionally, such behavior is referenced to the magnetic merit of Gd 3d being lower compared with Fe 3þ ions [46]; as will be explained in the next sections. Moreover, the diffraction rings identified by SAED images are analogous to the peaks (220), (113), (400), and (412) obtained by the XRD; see Fig. 1. These results emphasize the integrity between the HR-TEM and the XRD techniques in confirming the formation of pure cubic spinel phase of Gd 3d doped ZMF-nanoferrites.

4.3 FT-IR analysis

Figure 5 shows the FT-IR transmittance spectra obtained for ZMF0, ZMF1, ZMF2, ZMF3 and ZMF4 at room temperature in the range of 200–4000 cm^{-1}. The observed representative peaks confirmed the presence of the oxygen-containing functional groups at different Gd^{3+} ion concentrations of the composite and the characteristic absorption bands were obtained as well. The presence of these bands are mainly due to the vibrations of tetrahedral and octahedral metal–oxygen ions. The pure sample lies in frequency ν_1 equal 552.66 cm^{-1}, while the optimized sample ZMF4 lies at ν_1, ν_2 and ν_A cm^{-1} 551.14, 381.36 and 836.32, respectively [47, 48]. The first absorption band of

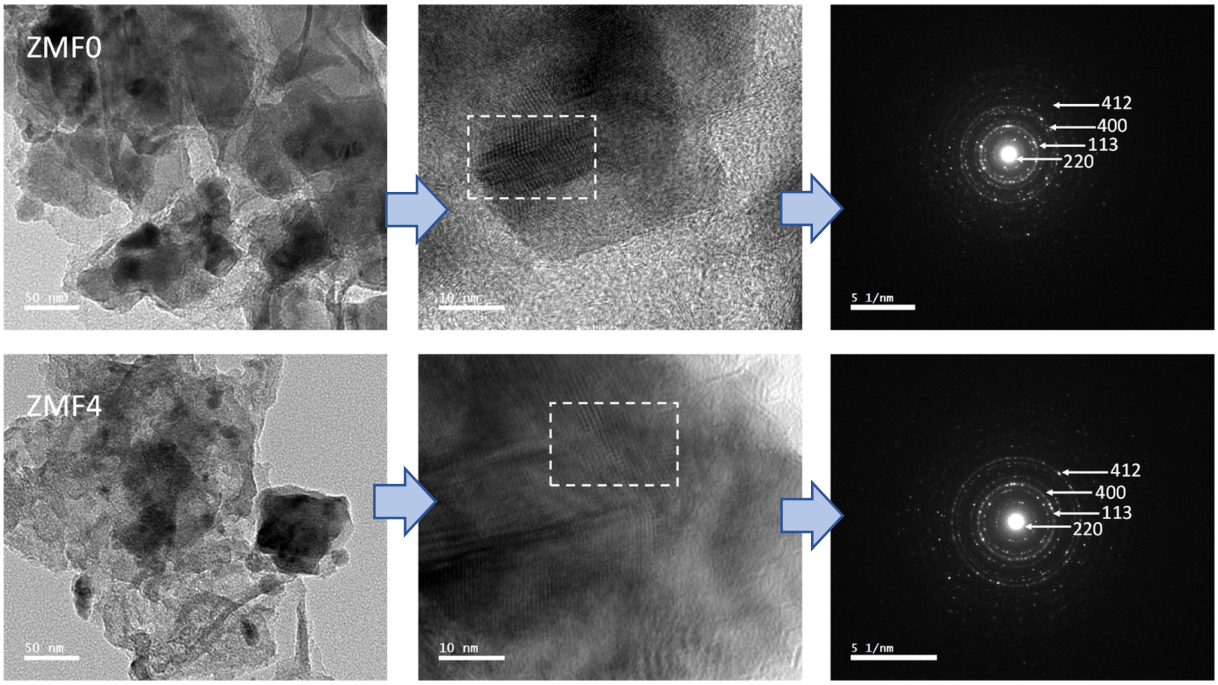

Fig. 4 HR-TEM and SEAD images of the ZMF0 and ZMF4 samples

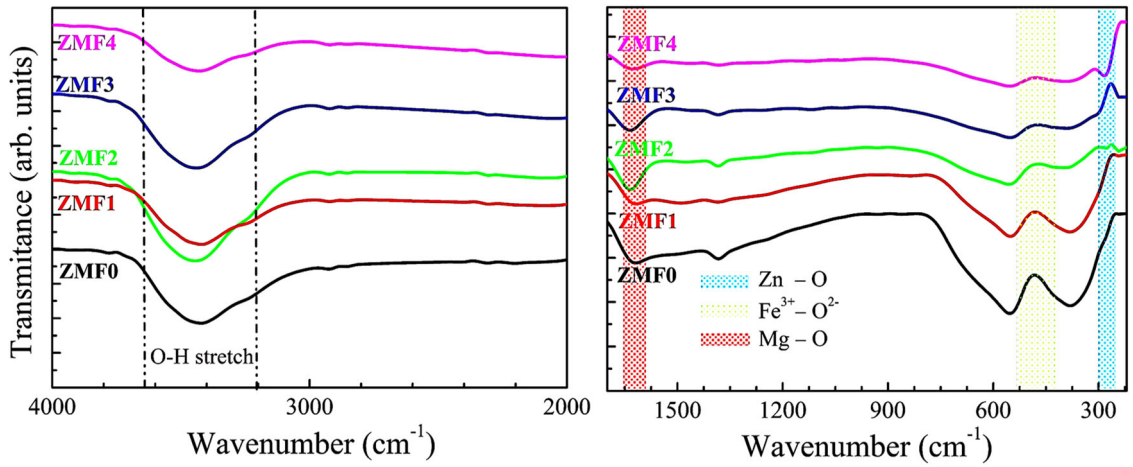

Fig. 5 FT-IR spectra for ZMF0, ZMF1, ZMF2, ZMF3 and ZMF4 spinel ferrite samples

the tetrahedral site, lied below 300 cm^{-1}, belongs to the stretching vibration of Zn–O [49], whilst, the second absorption band was confined by the range 440.14–575.68 cm^{-1} and corresponding to Fe^{3+}–O^{2-} [50] stretching vibrations. The third absorption band lied within the range 1557–1650 cm^{-1}, representing the Mg–O [51] stretching vibrations. Furthermore, the peaks obtained for different concentration ratios within the range 3300–3680 cm^{-1} which are assigned to O–H [52] deformation and O–H stretching vibrations in H–O–H [53] groups. The results of the FT-IR are presented in Table 2. The positions of the absorption bands were characterized by frequencies shift as the concentration ratio changed due to the cations redistribution and the distortion of crystal resulting from the substitution process [54]. When the Gd^{3+} ions were doped in the crystal structure, the replacement of Fe^{3+} by Gd^{3+} led to decrease in metal-oxygen bonds lengths that caused octahedral sites shifting towards higher frequencies as the Gd^{3+} ions have larger radii [55].

4.4 RAMAN analysis

RAMAN spectra of ZMF0, ZMF1, ZMF2, ZMF3 and ZMF4 spinel ferrite samples in the range of 25–2000 cm^{-1}

Table 2 FT-IR absorption band positions for ZMF-spinel ferrite samples

Sample	ν_1 (cm^{-1})	ν_2(cm^{-1})	ν_3(cm^{-1})	ν_4(cm^{-1})	ν_A(cm^{-1})	ν_B(cm^{-1})
ZMF0	552.66	390	–	–	1033.37	1119.71
ZMF1	552.88	380.64	–	242.41	861.65	929.75
ZMF2	553.31	393.64	283.51	–	–	1128.1
ZMF3	555.68	393.91	277.38	242.79	–	930
ZMF4	551.14	381.36	–	–	836.32	–

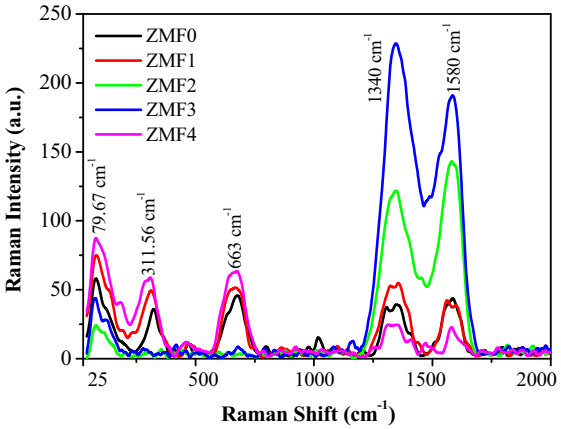

Fig. 6 RAMAN shift for ZMF0, ZMF1, ZMF2, ZMF3 and ZMF4 spinel ferrite samples

are shown in Fig. 6. The Figure shows different modes at 79.67, 311.56, 663, 1340 and 1580 cm^{-1} for all doping ratios of Gd^{3+}. The presence of the RAMAN band at 311.56 cm^{-1} was due to zinc ferrite nanoparticles associated with the α-Fe_2O_3 phase [56]. The Gd_2O_3 was synchronized in mode at 663.4 cm^{-1} [57]. A remarkable increase, high peaks, in RAMAN intensity as the Gd^{3+} doping ratios increased were found in the range between 1250–1750 cm^{-1} [58]. The presence of these peaks are attributed to the stretching vibration modes of the Gd_2O_3. This is a significant result showing the successful doping of Gd^{3+} ions within the structure which would affect its magneto-optical properties that will be discussed next in Sections 4.6 and 4.7.

4.5 X-ray photoelectron spectroscopy (XPS) analysis

The XPS spectra of Zn, Mg, Fe and O elements for ZMF0 and ZMF4 spinel ferrite samples are presented in Fig. 7. The cation distributions at different sites and binding energies obtained for ZMF0 and ZMF4 samples confirmed the presence of Zn(2p3), Mg(1 s), Fe(2p) and O(1 s) peaks, respectively. In the case of the A-site (tetrahedral) and B-site (octahedral) cation distributions, the analyses focus on the elements Zn and Fe. The Zn spectra exhibit two major peaks along with a satellite peak at a higher binding energy (BE) level. The Zn $2p_{3/2}$ peak, along with the satellite peak [59], indicate the presence of Zn^{2+} in the synthesized nanoparticles. The spectra obtained for Mg presented Mg 1 s peak for ZMF0 and ZMF4 confirming the presence of Mg^{2+} within the structure of the samples. On the other hand, the Fe 2p [60] spectra reveal the Fe $2p_{3/2}$ and Fe $2p_{1/2}$ peaks at higher (BE) levels. The existence of the Fe $2p_{3/2}$ peak suggests the presence of Fe^{3+} states in the synthesized nanoparticles. A sensitive variation in the binding energy of Fe^{3+} and Fe^{sat} peaks is observed when comparing the spectrum of ZMF4 to that of ZMF0. The spectral peak of O^{-2} $1S_{1/2}$ [61] at 529.61 eV for ZMF0 has been shifted to a higher binding energy as the Gd^{3+} content was increased in the optimized sample ZMF4 to 533.64 eV.

In Fig. 8 illustrated XPS spectra of the Gd^{3+} ions of ZMF1, ZMF2, ZMF3 and ZMF4 spinel ferrite samples. The shifting observed in the deconvoluted Gd $4d_{3/2}$ spectra provides compelling evidence that Gd^{3+} ions has been successfully doped within the synthesized structure where they've replaced the Fe^{3+} ions [62]. These results should affect the magneto-optical properties for the structure which will be discussed in the following sections. The XPS spectra survey of the ZMF0 and ZMF4 samples illustrated the elements Zn, Mg, Fe, C and O very clear, see Fig. 9. The basic spectrum for the pure sample ZMF0 confirmed the presence of Mg 1 s, Zn 2p3, Fe 2p, O 1 s and C 1 s, respectively. The Peaks obtained at around 712 eV and 1022 eV were found to characterized the Fe 2p and the Zn 2p3 electrons, respectively, meanwhile, the peak at 1304 eV was belonging to the Mg 1 s. This is in addition to the peaks observed in the spectrum found at 285, 531 identifying the C 1 s, O1s, respectively. Normally that, the Gd 4d peak is only observed for ZMF4 spectra at about 100 eV. All the XPS results are tabulated in Table 3.

4.6 UV spectroscopy analysis

The UV-VIS absorbance, absorption coefficient (α), Extinction coefficient *K* spectra were plotted as a function of the wavelength. Also, $(\alpha h\nu)^2$ was plotted against hν for the ZMF-spinel ferrite samples, Fig. 10a–d. The magnitudes elevations confirm the success doping of Gd^{3+} ions within the structure since they demonstrated the raise in energy absorbed by electrons offered by the dopant Gd^{3+} ions.

4.6.1 Absorption coefficient (α)

The spectral results obtained from UV-VIS spectroscopy within 340–500 nm range for the ZMF-spinel ferrite

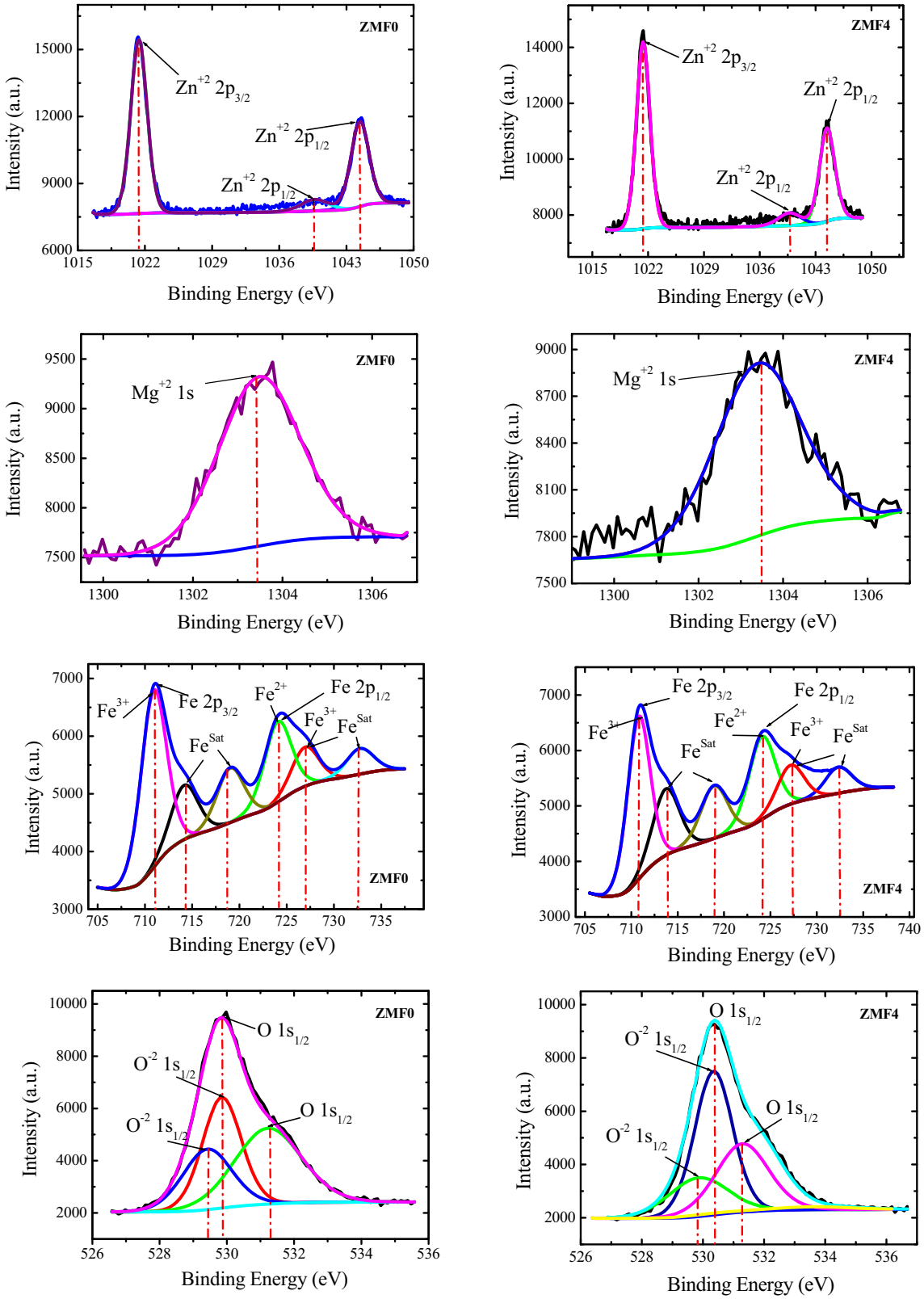

Fig. 7 XPS spectra of Zn, Mg, Fe and O elements for ZMF0 and ZMF4 spinel ferrite samples

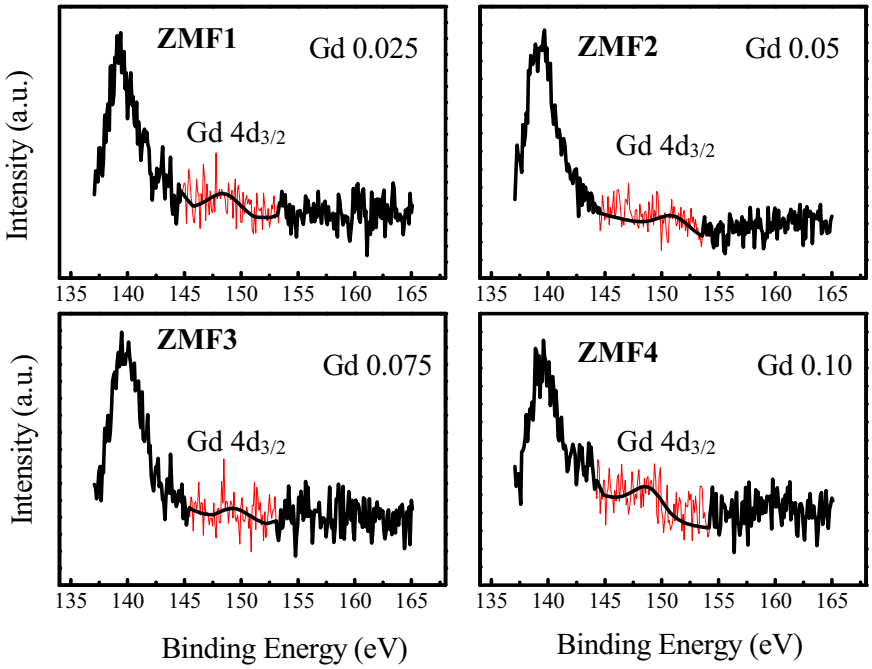

Fig. 8 XPS spectra of the Gd^{3+} ions of ZMF1, ZMF2, ZMF3 and ZMF4 spinel ferrite samples

samples were used to calculate the absorption coefficient (α) using Eq. (3)

$$\alpha = -\frac{\ln(1 - A)}{\tau} \tag{3}$$

Where A is the absorbance and τ is the optical length of the samples. According to Fig. 10b, "α" was increasing as the doping Gd^{3+} ions were raised within the structure of the samples. All samples showed superposed profiles for the intensity of absorbance hovering around 340 nm wavelength. This behavior was dramatically decreased to reach minimum value at 460 nm for all samples. Post 460 nm wavelength, the absorbance rate started to increase forming plateau behavior between 450 nm and 500 nm. The above results reveal that the ZMF-spinel ferrites working wavelength is 300–350 nm range. The Gd^{3+} ions have modulated the absorption properties of the spinel ferrite structure and the absorption magnitude depends upon the concentration ratio of the rare earth material. The enhancement of the electronic conduction within the structure has improved the electrical conduction of the material and hence approached probable electronic applications in use [63]. High energy photons capable of traveling between the valence and conduction bands could be generated according to the photo-excitation phenomena [64]. As the wavelength increased above 300 nm, the incident photons' energy became less, resulting in lower probabilities for electrons transitions between bands causing a drop in absorbance magnitude [65]. The maximum absorbance at ZMF4 leads to high ultraviolet photocatalytic [66] effective ability and vice-versa.

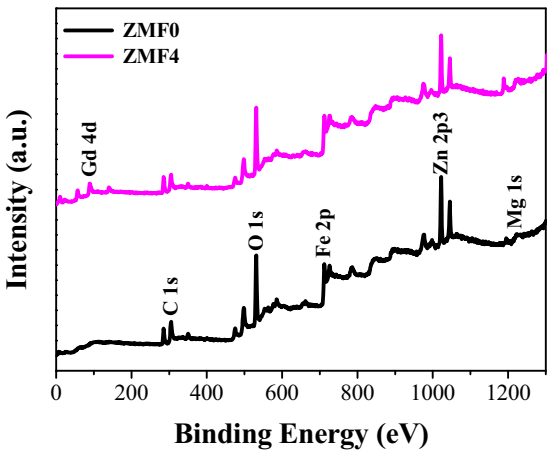

Fig. 9 XPS Survey of the ZMF0 and ZMF4 samples

4.6.2 Extinction coefficient, *k*

The variations in the extinction coefficient (k) with respect to the incident light wavelength were calculated for all ZMF-spinel ferrite samples, Fig. 10c, using Eq. (4):

$$k = \frac{\alpha\lambda}{4\pi} \tag{4}$$

"K" determines the radiation absorption/scatter percentage by the samples at certain wavelength. The values of "K" lie within $300\,\text{nm} < \lambda < 500\,\text{nm}$ range depending upon the concentration ratios of the Gd^{3+} within the samples. It is clear that (K) recorded a maximum value at a wavelength of 340 nm.

Table 3 XPS results for ZMF-spinel ferrite samples

Sample	Spectra	Peak BE	Height (CPS)	FWHM (eV)	Area CPS.eV	Atomic%	Sample name	Peak BE	Height (CPS)	FWHM (eV)	Area CPS.eV	Atomic%
ZMF0	**Zn2p**	1021.3	7785.9	2.01	16953.5	59.74	**ZMF4**	1021.3	6689.3	2.01	14604.6	59.05
	Zn2p- A	1044.4	3800.6	2.24	9228.2	33.53		1044.4	3331.5	2.27	8186.37	34.13
	Zn2p- B	1039.6	511.3	3.37	1864.72	6.73		1039.7	451.41	3.37	1646.29	6.82
	Mg1s	1303.4	1707.0	2.15	3979.9	100		1303.3	1107.9	2.4	2879.73	100
	Fe2p	714.16	941.31	3.37	3432.92	12.83		713.72	1197.3	3.37	4366.81	16.33
	Fe2p-A	726.93	678.83	3.37	2475.67	9.34		724.07	1491.1	3.37	5437.96	20.5
	Fe2p-B	724.06	1395.1	3.37	5088.06	19.16		718.92	947.8	3.37	3456.58	12.98
	Fe2p-C	719.03	942.77	3.37	3438.22	12.89		732.33	470.25	3.37	1714.97	6.51
	Fe2p-D	732.74	445.11	3.37	1623.28	6.15		727.17	701.72	3.37	2559.14	9.67
	Fe2p-E	710.91	3070.6	3.2	10633.4	39.63		710.79	2932.1	2.87	9114.29	34.01
	O1s	529.78	4092.6	1.37	6056.45	33.05		529.78	5242.4	1.46	8294.81	46.87
	O1s-A	531.22	2904	2.34	7347.88	40.13		531.39	2304.3	2	4998.13	28.27
	O1s-B	529.61	2303.1	1.97	4914.71	26.82		533.64	102.46	2.72	302.01	1.71
	O1s-C							529.86	1506.2	2.51	4097.36	23.15

Binding energy for Gd^{3+}

Sample	**Spectra**	**Peak BE**	**Height (CPS)**	**FWHM (eV)**	**Area (CPS.eV)**	**Atomic%**
ZMF1	**Gd4d**	148.52	68.54	3.39	249.95	100
ZMF2	**Gd4d**	151.05	45.85	3.37	167.2	100
ZMF3	**Gd4d**	149.36	45.17	3.46	164.72	100
ZMF4	**Gd4d**	148.85	76.14	3.37	277.67	100

Survey

Sample	**Specta**	**Peak BE**	**Height CPS**	**FWHM eV**	**Area CPS.eV**	**Atomic %**
ZMF0	**Zn2p3**	1022.01	41649.55	3.21	163308.3	9.3
	Mg1s	1303.95	11248.89	3.75	58479.58	9.87
	Fe2p	712.1	22615.73	4.99	240278.46	11.61
	O1s	531.02	43426.58	3.66	180467.22	43.07
	C1s	285.33	9252.21	3.62	42897.16	26.15
ZMF4	**Zn2p3**	1022.06	35914.86	3.29	142864.66	8.81
	Mg1s	1304.03	7540.71	3.54	32936.25	6.02
	Gd4d	148.85	76.14	3.37	277.67	020
	Fe2p	711.99	21324.71	5.56	246326.13	12.87
	O1s	531.03	41350.14	3.7	172600.18	44.57
	C1s	285.41	9712.59	3.46	42048.16	27.73

4.6.3 Optical energy band gap, Eg

The optical band gaps were calculated according to Tauc's relation represented by Eq. (5). Moreover, the results obtained were plotted between αhν vs. hν in Fig. 10d:

$$\alpha h\nu = A(h\nu - Eg)^n \quad (5)$$

Where A is a constant, h (J.s) is the Planck's constant, ν (Hz) is the incident light frequency, Eg (eV) is the optical band gap energy and "n" is a power factor that equals to 1/2 for the direct band gap semiconductor materials [67]. The results obtained for the optical band gaps of ZMF-samples were found to decrease from 3.21 eV to 2.99 eV as the doping ratios of the Gd^{3+} ions were increased, Table 4. The resulting blue shift [68] of the band edge absorption in ZMF-spinel ferrites can be explained following the probabilities of both charge transfer and d-d transitions [69] within the iron (Fe) d-orbitals. A smaller band gap promotes such transitions, potentially leading to bluer light emission. This can be complex and vary depending on Gd^{+3} ions substitution probabilities. These results are in consistent with those obtained in the previous XPS section.

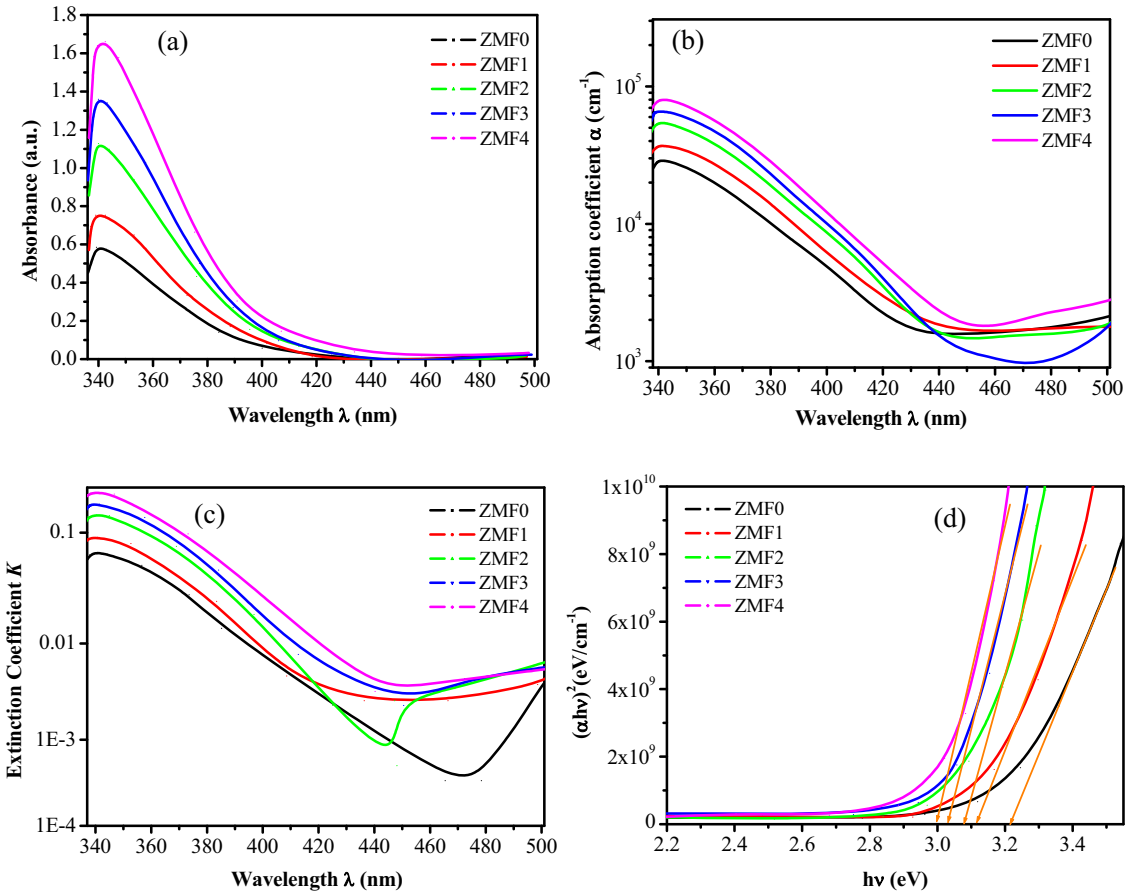

Fig. 10 UV-VIS (**a**) absorbance, (**b**) absorption coefficient (α), (**c**) Extinction coefficient *K* and (**d**) $(\alpha h\nu)^2$ vs. h*ν* spectra for ZMF0, ZMF1, ZMF2, ZMF3 and ZMF4 spinel ferrite samples

Table 4 The Energy Gap values for ZMF-spinel ferrite samples

Sample	Band gap (eV)
ZMF0	3.21
ZMF1	3.11
ZMF2	3.07
ZMF3	3.02
ZMF4	2.99

4.7 Magnetic measurements

The hysteresis loops of the prepared spinel nano-ferrites ZMF0, ZMF1, ZMF2, ZMF3 and ZMF4 at room temperature under the magnetic field in the range of ±20 KOe were shown in Fig. 11. The magnetic parameters including saturation magnetization, M_s, coercivity, H_c and remnant magnetization, M_r obtained from the hysteresis loops are listed in Table 5. In addition, the squareness ratio, M_r/M_s, anisotropy constant, K, and the magnetic moment, μ_B, were calculated using the following equations and presented in Table 5 as well:

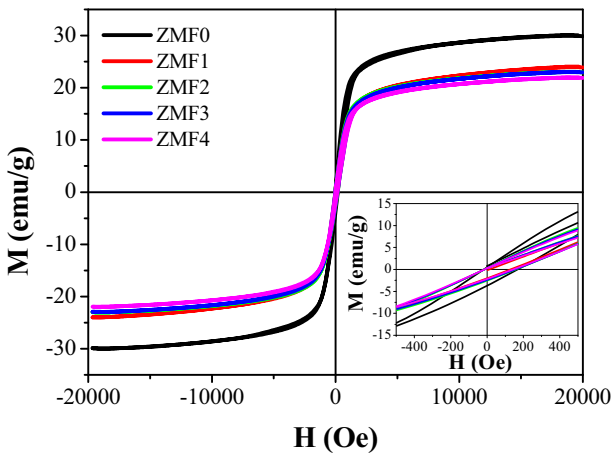

Fig. 11 The magnetic hysteresis loops (M-H loop) for ZMF0, ZMF1, ZMF2, ZMF3 and ZMF4 spinel ferrite samples

$$K = \frac{H_c M_s}{0.96} \tag{6}$$

Table 5 Saturation magnetization (Ms), Remanent magnetization (Mr), Coercivity (Hc), Squareness ratio (M_r/M_S), Effective magnetic anisotropy (K_{eff}) and Bohr magneton (μ_B)

Sample	M_S (emu/g)	M_r (emu/g)	H_C (Oe)	$M_r/M_S \times 10^{-3}$	$K \times 10^{-3}$ (erg/Oe)	β (μ_B)
ZMF0	30.04	2.99	110.95	99.70	3.47	1.186
ZMF1	24.03	2.01	103.52	87.15	2.49	0.932
ZMF2	23.08	1.91	101.33	83.13	2.43	0.940
ZMF3	23.02	1.73	95.69	78.76	2.19	0.909
ZMF4	21.99	1.63	87.69	67.69	2.19	0.959

$$S = \frac{M_R}{M_s} \tag{7}$$

$$\mu_B = \frac{MWxM_s}{5585} \tag{8}$$

Where 5585 is the magnetic factor and MW is the molecular weight. It is noticed that the coercivity, H_C, values have decreased from 110.95 Oe to 87.69 Oe as the Gd^{3+} ions were increased. The decrease in H_C is interpreted as a consequence of the cation arrangements over the tetrahedral A and octahedral B sites [70]. The magnetocrystalline anisotropy constant (K) is a crucial parameter that describes the dependence of magnetic properties on a material's crystallographic orientation. It is essential for understanding the magnetic behavior and performance of ferrites, especially when rare earth (RE) elements are introduced. RE elements possess large single-ion anisotropy due to their unpaired 4f electrons, which, when substituted into the octahedral sites of the ferrite lattice, contribute significantly to the overall magnetocrystalline anisotropy of the material, resulting in an increased K. This enhancement enhances the magnetic hardness and stability of the ferrite, making it suitable for high-performance magnetic applications. RE-substituted ferrites exhibit a higher magnetocrystalline anisotropy constant compared to pure ferrites, due to strong spin-orbit coupling and the large orbital contributions of RE ions. In conclusion, RE-substituted ferrites are ideal for high-performance magnetic applications due to their enhanced anisotropic properties. The magnetic order in spinel ferrites is mainly referenced to the superexchange interactions built up among these tetrahedral and octahedral sites through oxygen ions [71]. Rare earth metals have always been recognized as strong paramagnetic in normal temperature conditions [72]. As a result of having larger ionic radii, Gd^{3+} ions (0.938 Å) become competent to occupy the B sites in trade with smaller Fe^{3+} ions (0.67 Å). Such trading lead to reduce the total magnetic moment at these sites that yield finally a net reduction in coercivity as the non-magnetic Gd^{3+} doped ions were increased. Furthermore, M_S and M_r were found to decrease from 30.04 to 21.99 and 2.99 to 1.63 for pure sample and ZMF4 respectively. Also, the squareness ratio was found to fall from 99.70×10^{-3} to 67.69×10^{-3} for these two samples as well. All magnitudes drops were noticed to occur as increasing the Gd^{3+} concentration ratios within the samples. The results obtained for M_S is ascribed to the attenuation of the Fe^{3+}– Fe^{3+} interactions in parallel with the weak Gd^{3+}–Fe^{3+} and Gd^{3+}– Gd^{3+} interchanges [72].

The dM/dH curves for ZMF-spinel ferrite samples ZMF0, ZMF1, ZMF2, ZMF3 and ZMF4 are shown in Fig. 12. The width of dM/dH curves was kept constant and overlapped for all of Gd^{3+} ions doping ratios. Furthermore, the magnitude of the dM/dH peaks were dropped from 0.035 for ZMF0 to about 0.025 for the rest of all doped samples. This behavior is mainly referenced to the presence of the superparamagnetic [73, 74] regions within the structure as the Gd^{3+} ions concentrations were raised which, in turn, enhanced the magnetic properties of the composite in the direction of soft magnetic. It is noted that the magnetization has improved at higher field of 20 KOe which can be attributed to the superparamagnetic behavior of nanoparticles [75, 76]. Based on the enhanced magnetization status observed in the ZMF-spinel ferrite samples by changing the doping of rare earth Gd^{3+}ratios, several high-tech applications can be envisioned such as transformers, inductors, magnetic recording media, and magnetic sensors.

4.8 Radiation properties

4.8.1 FLUKA simulation study

In this study, the potent Monte Carlo method called FLUKA (**FLU**ktuierende **KA**skade) is used to calculate the radiation shielding efficacy of the given nanomaterial. The robust Monte Carlo technique may be helpful in many disciplines due to the expensive costs of laboratory equipment and, of course, the lack of access to it. This code exploits the FLAIR (**FL**UKA **A**dvanced **I**nte**R**face) [77–80] to simplify the editing process, running code, and visualization of the outcomes. This program can simulate the transportation of over sixty particles, including electrons, neutrinos, neutrons, photons, heavy ions, and muons, in wide energy ranges. The FLUKA code version 2011.2x-4 and FLAIR version 2.3 have been used in this work to investigate the radiation shielding efficiency of the selected nanomaterial. In the FLUKA environment, an isotropic spherical photon source spanning from 0.1 to 10 MeV is simulated using BEAM and two BEAMPOS cards. Type: positive, and Type: SPH-VOL with the inner and outer radius of $r_{in} = 0$, $r_{out} = 0.5$ cm are selected for the first and second BAMPOS cards, respectively. Additionally, three

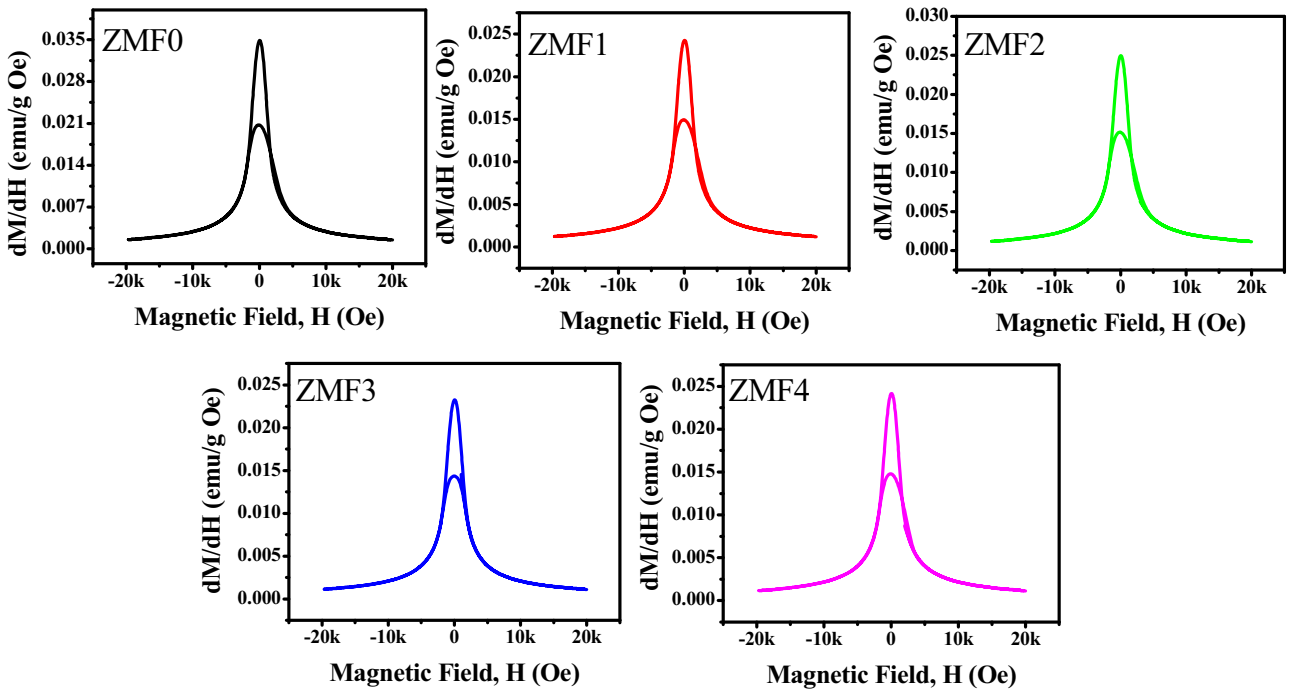

Fig. 12 dM/dH vs. Magnetic Field H (Oe) for ZMF0, ZMF1, ZMF2, ZMF3 and ZMF4 spinel ferrite samples

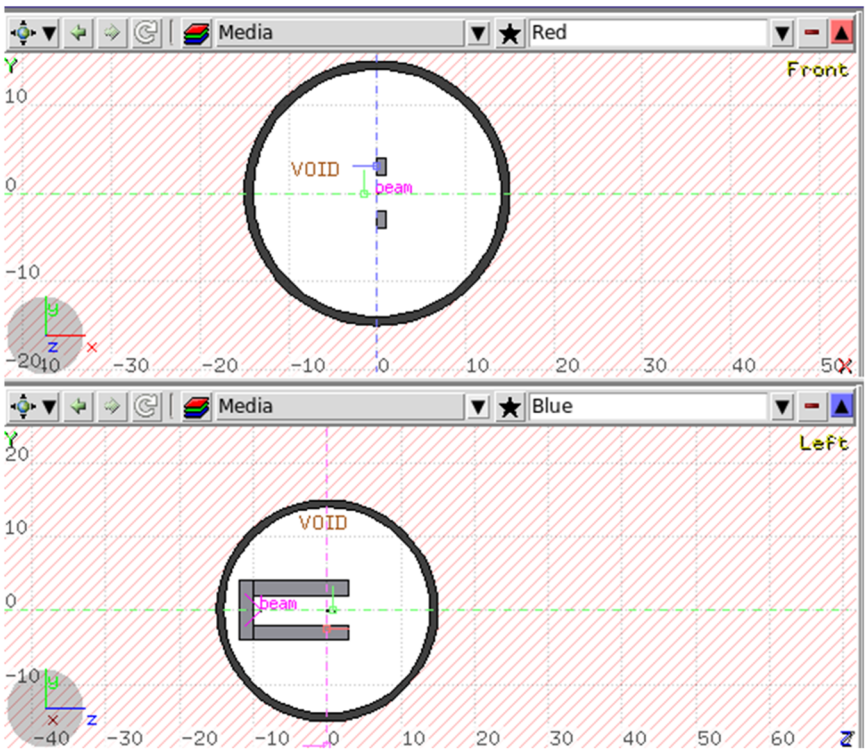

Fig. 13 Front and left views of the simulation study

cm thick lead volumes are simulated around the source and sample. The dimensions of the simulated equipment have been derived from an experimental sample in the reference [81–83] that was previously used to test the protection properties of samples. All geometry is encased within BLKBODY shell, with a radius of 13 cm from GEOBEGIN to GEOEND. Ten centimeters away from the photon source, the nanomaterial with a radius of 900 nanometers is

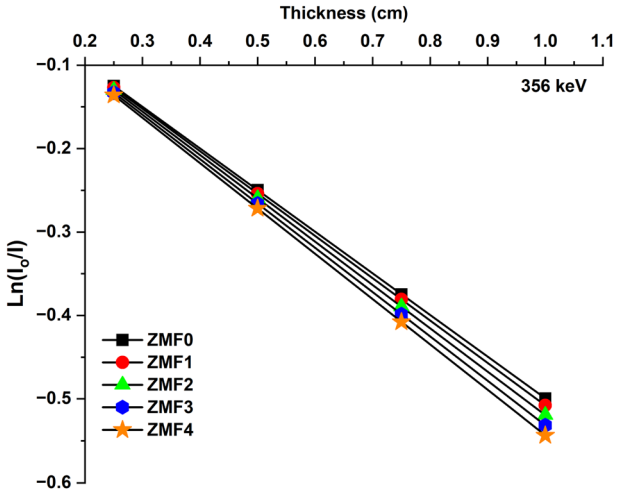

Fig. 14 The Io/I ratio of the samples at 356 keV against the thickness of the samples

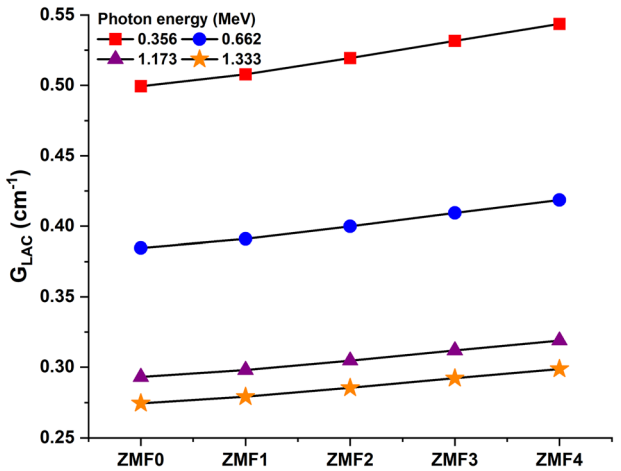

Fig. 15 The linear attenuation coefficient (G_{LAC}) versus Gd content for samples

simulated. The density of the samples has been entered into the MATERIAL card, and the weight percentages of the material have been added using COMPOUNDS (f1: to f6:) in the FLUKA input file. The simulation system used in this experiment for front and left views are depicted in Fig. 13. Furthermore, spheric volumes are created before and after the sample, and the flux is obtained by applying the USRTRACK (type: linear, part: photon) card. The attenuation factors can be calculated by comparing the initial flux (before the sample) and final flux (after the sample) using Beer Lambert's Law. The aforementioned cards ensure that the properties and behavior of the simulated nanomaterials closely resemble those of their real-world counterparts, resulting in reliable and relevant radiation shielding predictions.

To obtain the Cs-137 and Co-60 spectra using FLUKA Monte Carlo code, Hi-PROPE card is used [84, 85]. In this card, the atomic number and mass number of the radioactive source should be added. This card will be used with RADDECAY and DCYSCORE card for each scoring cards and particles. Adding a Semi-analog and kind of the scoring, the gamma photon spectrum can be obtained for each sample. Additionally, USRTRACK scoring cards have been used for wide energy ranging from 0.001 to 1.5 MeV, 100 million primaries, and 5 cycles to minimize errors.

4.8.2 Radiation shielding study

The Ln (I_o/I) ratio of the samples at 356 keV is shown against the sample thickness Fig. 14. In the beginning, the ratio is −0.02, which is the largest value. This indicates that all radiation is able to pass through the samples; however, as the thickness of the samples increases, the ratio significantly falls. These samples have a larger thickness, which causes a bigger proportion of the incoming photons to get trapped inside the material, which ultimately results in a greater attenuation. At each and every thickness, the sample that has the maximum amount of Gd has the ratios that are the lowest (more attenuation). To put it another way, increasing the concentration of Gd in the samples means that the I_o/I ratio of the samples may be reduced even more at a certain thickness. As a consequence of this, the sample that has the greatest Gd (1 weight percent) also has the lowest I_o/I value across all thickness groups.

In Fig. 15, the variations in G_{LAC} are shown in relation to the concentration of Gd. This figure serves as a sample example for the lower and higher energy ranges of 0.356–1.333 MeV. The data that has been provided demonstrates that Gd additives have a significant impact on the values of the G_{LAC}, which demonstrate an upward trend in the range of energies that range from 0.356 to 1.333 MeV between the small and high energies. In point of fact, these behaviors may be rationalized by the influence that Gd has on the structural features of samples, such as raising the densities of the samples. The density of a medium has been considered an important factor that plays a role in the medium's capacity to reduce the amount of radiation photons that it absorbs. It is also important to note that the G_{LAC} is dependent not only on the mass of the photons but also on their energy. To go into further detail, the photon energy had an effect on the rate at which the G_{LAC} altered in response to changes in density.

For each of the varied Gd concentrations, the G_{MAC} findings for the samples were computed and presented in the form of a photon energies function shown in Fig. 16. For all samples, the GMAC values decrease with increasing the photon energy. In addition, the sample that has 1.0 wt% of Gd has the highest value of G_{MAC}.

According to the data that are provided in Fig. 17, it is clear that the G_{HVL} values decrease as the concentration of

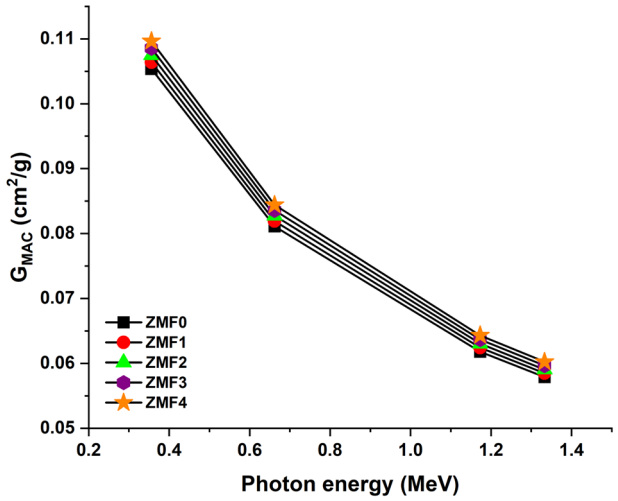

Fig. 16 The mass attenuation coefficient (G_{MAC}) versus photon energy for samples

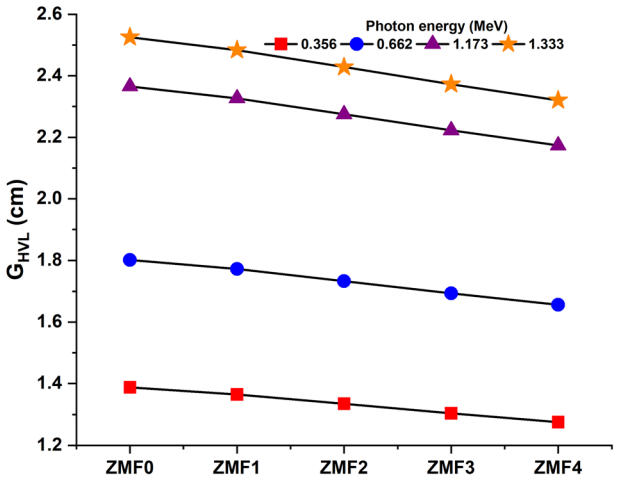

Fig. 17 The half value layer (G_{HVL}) versus Gd content for samples

Gd increases from 0 to 1 weight percent within the range of low and high photon energy, which is from 0.356 to 1.333 MeV. One possible explanation for these reductions is that the shielding material densities have an inverse reliance on both G_{HVL} and the shielding material density. It is clear that the G_{HVL} values have decreased as a direct consequence of the rise in density values. In addition, the lower G_{HVL} values indicate that the barrier against nuclear radiation dangers has been increased in effectiveness and efficiency. Based on this discovery, it seems that the presence of Gd has a considerable influence on the shielding capability of the samples that are currently known to exist.

Furthermore, the nuclear photon build-up factor must be taken into consideration when dealing with nuclear data, such as radiation shielding and dosimetry. The build-up factor is equivalent to the proportion of the target that is contributed by photons that collide with one another. To this investigation, the geometry progressive (G-P) approach was used to ascertain the values of the exposure build-up factor (EBF) and the energy absorption build-up factor (EABF). You may get the specific details on the G-P approach in a publication that was conducted in the past [86]. For this reason, the fluctuation of EBF and EABF with incoming photon energies is shown in Figs. 18a, b and 19a, b, respectively, for samples ZMF0 and ZMF4, with penetration depths of 5, 10, 20, and 40 mfp (as an example). As the input energy declines, the depth-dependent absorption increases until it reaches a maximum value in the intermediate energy field, at which point it decreases. This continues until it achieves a constant value. The majority of gamma-ray absorption takes place in the low (photoelectric dominating) and high (pair formation dominating) energy ranges, which are conditions in which the accumulation of particles is restricted significantly. On the other hand,

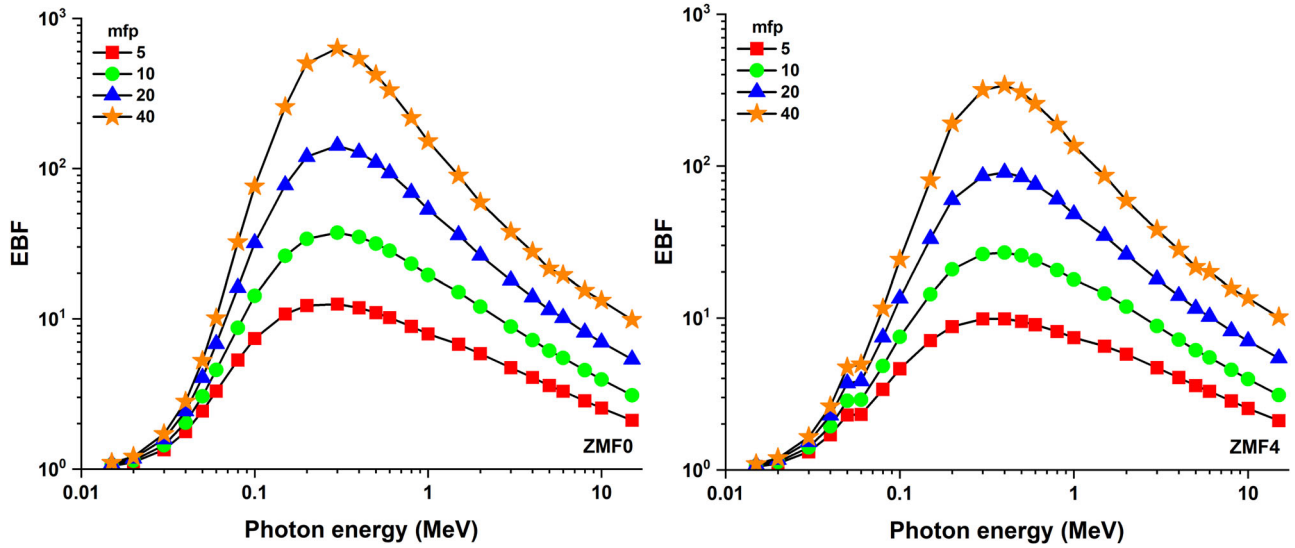

Fig. 18 Exposure buildup factor (EBF) versus photon energy at different mean free path of ZMF0 and ZMF4 samples

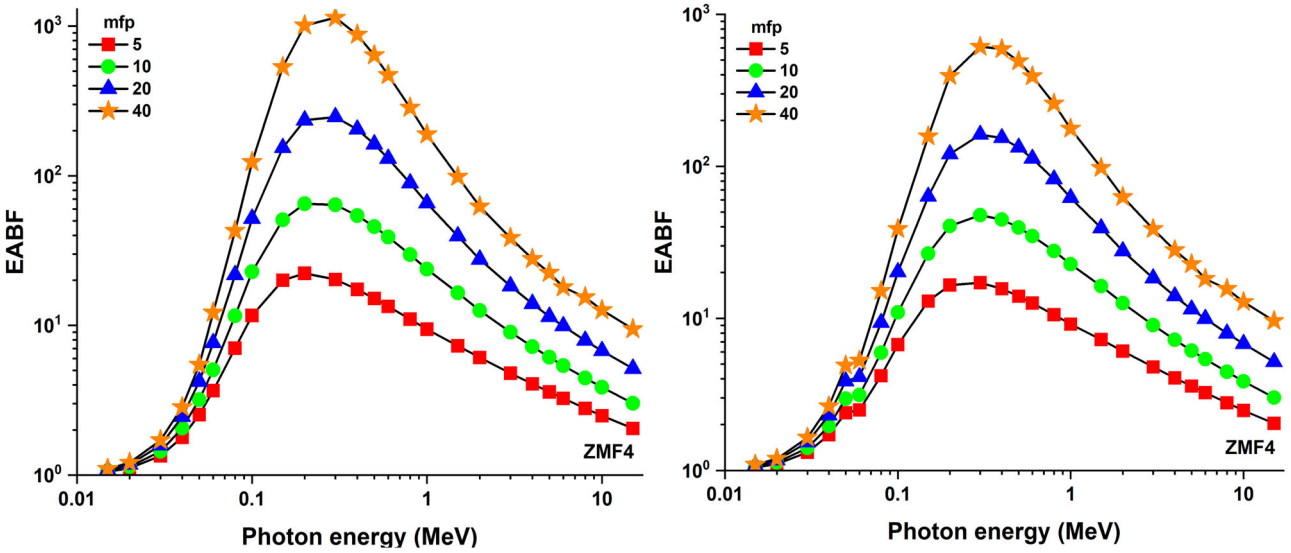

Fig. 19 Energy absorption buildup factor (EABF) versus photon energy at different mean free path of ZMF0 and ZMF4

Table 6 (EBF and EABF) G–P fitting coefficients (b, c, a, X_k and d) of ZMF0 sample

E (MeV)	Z_{eq}	EBF					EABF				
		a	b	c	d	X_k	a	b	c	d	X_K
0.015	13.69	0.245	1.025	0.363	−0.167	13.059	0.205	1.024	0.399	−0.106	12.065
0.020	14.06	0.179	1.050	0.426	−0.106	17.411	0.180	1.050	0.425	−0.107	17.396
0.030	14.49	0.214	1.160	0.394	−0.116	14.201	0.217	1.160	0.392	−0.120	14.134
0.040	14.76	0.193	1.331	0.444	−0.108	14.407	0.193	1.340	0.443	−0.107	14.648
0.050	14.95	0.161	1.538	0.523	−0.089	14.710	0.154	1.578	0.529	−0.083	15.316
0.060	15.10	0.119	1.739	0.627	−0.065	14.764	0.165	1.958	0.539	−0.086	13.861
0.080	15.30	0.081	2.130	0.759	−0.049	13.550	0.105	2.693	0.702	−0.071	13.405
0.100	15.44	0.040	2.363	0.908	−0.042	13.587	0.047	3.329	0.887	−0.047	13.650
0.150	15.65	−0.018	2.533	1.155	−0.018	12.284	−0.030	3.874	1.196	−0.007	15.322
0.200	15.78	−0.041	2.519	1.280	−0.012	10.556	−0.059	3.687	1.354	0.007	18.962
0.300	15.93	−0.057	2.409	1.368	−0.008	8.574	−0.082	3.150	1.477	0.019	16.040
0.400	16.02	−0.071	2.285	1.416	0.015	20.348	−0.082	2.840	1.475	0.019	16.918
0.500	16.06	−0.073	2.199	1.414	0.015	16.469	−0.085	2.600	1.475	0.022	15.543
0.600	16.09	−0.070	2.133	1.391	0.016	18.099	−0.083	2.445	1.453	0.023	15.689
0.800	16.11	−0.066	2.027	1.352	0.017	16.587	−0.075	2.252	1.394	0.022	15.397
1.000	16.11	−0.061	1.949	1.312	0.017	15.860	−0.066	2.129	1.336	0.021	15.580
1.500	11.65	−0.049	1.871	1.233	0.017	14.755	−0.053	1.939	1.250	0.020	14.432
2.000	10.28	−0.034	1.804	1.156	0.013	14.635	−0.035	1.844	1.157	0.013	14.722
3.000	9.95	−0.011	1.692	1.055	0.001	11.226	−0.010	1.707	1.051	0.000	11.801
4.000	9.87	0.005	1.612	0.991	−0.008	15.458	0.008	1.616	0.984	−0.010	13.095
5.000	9.83	0.016	1.542	0.953	−0.017	14.924	0.019	1.547	0.945	−0.014	12.886
6.000	9.81	0.029	1.498	0.915	−0.024	12.918	0.026	1.489	0.921	−0.027	15.649
8.000	9.78	0.033	1.410	0.898	−0.024	13.075	0.032	1.397	0.900	−0.021	12.298
10.000	9.76	0.042	1.351	0.875	−0.030	13.490	0.038	1.336	0.884	−0.028	13.919
15.000	9.75	0.059	1.264	0.830	−0.050	14.608	0.042	1.238	0.875	−0.034	14.731

Compton scattering is the mechanism that is seen the most often for photon-matter interaction at intermediate energies; nevertheless, it is not the mechanism that is observed for absolute photon loss. Therefore, the EBF values are highest in the Compton area as a consequence of this. In addition to the fact that EBF levels vary from area to region, it was discovered

Table 7 (EBF and EABF) G–P fitting coefficients (b, c, a, X_k and d) of ZMF1 sample

E (MeV)	Z_{eq}	EBF					EABF				
		a	b	c	d	X_k	a	b	c	d	X_K
0.015	13.78	0.250	1.024	0.359	−0.171	12.733	0.201	1.023	0.404	−0.097	11.792
0.020	14.17	0.178	1.049	0.427	−0.103	16.990	0.182	1.049	0.423	−0.106	16.947
0.030	14.61	0.214	1.156	0.394	−0.115	14.250	0.217	1.156	0.392	−0.121	14.072
0.040	14.89	0.194	1.322	0.441	−0.108	14.419	0.193	1.330	0.441	−0.107	14.654
0.050	15.09	0.163	1.525	0.517	−0.091	14.683	0.158	1.564	0.521	−0.085	15.193
0.060	15.84	0.136	1.653	0.585	−0.076	14.653	0.141	1.772	0.571	−0.076	15.001
0.080	16.13	0.077	1.949	0.755	−0.046	14.874	0.129	2.501	0.640	−0.083	13.174
0.100	16.33	0.052	2.219	0.859	−0.044	13.254	0.068	3.097	0.816	−0.057	13.548
0.150	16.65	−0.008	2.412	1.102	−0.021	12.871	−0.010	3.741	1.112	−0.018	13.080
0.200	16.86	−0.031	2.432	1.227	−0.015	11.455	−0.043	3.644	1.277	−0.004	16.368
0.300	17.10	−0.051	2.346	1.335	−0.010	8.503	−0.071	3.157	1.419	0.015	19.081
0.400	17.24	−0.060	2.253	1.370	0.000	12.740	−0.077	2.833	1.444	0.017	16.781
0.500	17.33	−0.068	2.163	1.390	0.017	20.313	−0.078	2.610	1.441	0.019	16.625
0.600	17.38	−0.067	2.102	1.376	0.015	18.658	−0.077	2.452	1.423	0.020	16.674
0.800	17.43	−0.065	2.004	1.344	0.017	16.554	−0.072	2.249	1.380	0.021	15.591
1.000	17.44	−0.060	1.932	1.306	0.017	15.982	−0.066	2.121	1.335	0.021	15.114
1.500	12.38	−0.049	1.862	1.232	0.017	15.096	−0.053	1.940	1.247	0.020	14.591
2.000	10.52	−0.034	1.801	1.155	0.012	14.567	−0.034	1.844	1.156	0.013	14.732
3.000	10.07	−0.011	1.691	1.055	0.001	11.137	−0.010	1.707	1.051	0.000	11.663
4.000	9.96	0.005	1.612	0.991	−0.008	15.234	0.008	1.616	0.984	−0.010	13.101
5.000	9.91	0.016	1.542	0.953	−0.017	14.944	0.019	1.547	0.945	−0.014	12.870
6.000	9.88	0.029	1.498	0.915	−0.024	12.815	0.026	1.488	0.921	−0.027	15.670
8.000	9.85	0.033	1.410	0.898	−0.024	13.103	0.032	1.396	0.901	−0.021	12.297
10.000	9.83	0.042	1.351	0.875	−0.031	13.473	0.038	1.335	0.884	−0.028	13.919
15.000	9.81	0.059	1.264	0.830	−0.050	14.594	0.042	1.237	0.876	−0.034	14.731

Table 8 (EBF and EABF) G–P fitting coefficients (b, c, a, X_k and d) of ZMF2 sample

E (MeV)	Z_{eq}	EBF					EABF				
		a	b	c	d	X_k	a	b	c	d	X_K
0.015	13.83	0.253	1.024	0.356	−0.173	12.556	0.198	1.023	0.407	−0.093	11.643
0.020	14.22	0.178	1.049	0.427	−0.101	16.780	0.182	1.049	0.423	−0.105	16.723
0.030	14.67	0.214	1.153	0.394	−0.115	14.273	0.218	1.154	0.392	−0.121	14.043
0.040	14.94	0.195	1.318	0.440	−0.108	14.425	0.194	1.325	0.440	−0.107	14.657
0.050	15.15	0.164	1.519	0.515	−0.091	14.678	0.159	1.558	0.518	−0.086	15.159
0.060	16.43	0.146	1.595	0.561	−0.082	14.567	0.142	1.686	0.563	−0.078	15.280
0.080	16.78	0.089	1.872	0.719	−0.052	14.699	0.144	2.369	0.604	−0.090	13.292
0.100	17.04	0.055	2.101	0.839	−0.042	13.804	0.085	2.930	0.765	−0.066	13.439
0.150	17.43	−0.001	2.319	1.065	−0.023	13.183	0.004	3.633	1.050	−0.025	13.310
0.200	17.69	−0.024	2.370	1.189	−0.018	11.899	−0.031	3.611	1.220	−0.012	13.292
0.300	18.01	−0.048	2.298	1.312	−0.011	9.026	−0.064	3.161	1.377	0.012	21.138
0.400	18.19	−0.053	2.230	1.337	−0.010	8.385	−0.073	2.831	1.419	0.015	17.343
0.500	18.30	−0.065	2.138	1.373	0.017	21.850	−0.073	2.619	1.416	0.017	17.287
0.600	18.38	−0.065	2.081	1.363	0.014	18.657	−0.073	2.456	1.405	0.018	16.805
0.800	18.45	−0.063	1.987	1.335	0.015	16.699	−0.069	2.255	1.365	0.019	16.169
1.000	18.46	−0.058	1.920	1.299	0.016	15.936	−0.064	2.123	1.324	0.019	15.197
1.500	13.07	−0.048	1.854	1.230	0.017	15.944	−0.052	1.940	1.245	0.020	14.695
2.000	10.80	−0.034	1.797	1.155	0.012	14.487	−0.034	1.845	1.155	0.013	14.742
3.000	10.25	−0.011	1.690	1.055	0.001	11.006	−0.009	1.707	1.050	−0.001	11.459
4.000	10.12	0.005	1.611	0.991	−0.008	14.865	0.008	1.616	0.984	−0.011	13.110
5.000	10.05	0.016	1.541	0.953	−0.018	14.980	0.019	1.546	0.945	−0.014	12.842
6.000	10.02	0.029	1.497	0.915	−0.024	12.627	0.025	1.487	0.922	−0.027	15.710
8.000	9.98	0.033	1.409	0.899	−0.024	13.155	0.032	1.395	0.901	−0.021	12.295
10.000	9.96	0.042	1.350	0.875	−0.031	13.439	0.038	1.334	0.886	−0.028	13.921
15.000	9.94	0.060	1.264	0.829	−0.051	14.566	0.041	1.236	0.878	−0.034	14.730

Table 9 (EBF and EABF) G–P fitting coefficients (b, c, a, X_k and d) of ZMF3 sample

E (MeV)	Z_{eq}	EBF					EABF				
		a	b	c	d	X_k	a	b	c	d	X_K
0.015	13.90	0.257	1.024	0.353	−0.175	12.312	0.195	1.023	0.410	−0.086	11.439
0.020	14.30	0.178	1.048	0.428	−0.098	16.474	0.184	1.048	0.421	−0.104	16.397
0.030	14.75	0.214	1.150	0.394	−0.115	14.308	0.218	1.151	0.391	−0.121	13.999
0.040	15.04	0.195	1.312	0.438	−0.109	14.436	0.195	1.319	0.438	−0.108	14.663
0.050	15.24	0.166	1.510	0.512	−0.092	14.670	0.162	1.549	0.514	−0.087	15.107
0.060	17.01	0.155	1.542	0.541	−0.086	14.485	0.149	1.624	0.542	−0.082	15.333
0.080	17.42	0.101	1.801	0.685	−0.057	14.535	0.158	2.244	0.570	−0.095	13.402
0.100	17.71	0.058	1.995	0.821	−0.041	14.299	0.100	2.780	0.719	−0.073	13.342
0.150	18.18	0.005	2.235	1.034	−0.024	13.455	0.018	3.531	0.994	−0.033	13.463
0.200	18.47	−0.021	2.293	1.171	−0.017	11.988	−0.021	3.566	1.170	−0.018	12.462
0.300	18.84	−0.044	2.260	1.287	−0.011	9.974	−0.050	3.184	1.320	−0.006	11.092
0.400	19.07	−0.049	2.208	1.314	−0.011	8.921	−0.067	2.841	1.387	0.014	20.498
0.500	19.20	−0.060	2.123	1.350	0.009	18.496	−0.069	2.625	1.394	0.014	17.446
0.600	19.28	−0.062	2.067	1.347	0.013	19.812	−0.070	2.462	1.387	0.017	17.708
0.800	19.37	−0.061	1.973	1.326	0.015	17.673	−0.066	2.262	1.350	0.017	16.561
1.000	19.39	−0.057	1.910	1.292	0.015	16.338	−0.060	2.128	1.309	0.017	15.827
1.500	13.74	−0.048	1.845	1.230	0.016	15.341	−0.051	1.941	1.242	0.019	14.464
2.000	11.05	−0.034	1.795	1.154	0.012	14.523	−0.034	1.844	1.155	0.013	14.732
3.000	10.40	−0.011	1.689	1.055	0.001	10.897	−0.009	1.707	1.050	−0.001	11.291
4.000	10.24	0.006	1.610	0.992	−0.008	14.572	0.008	1.616	0.984	−0.011	13.117
5.000	10.17	0.016	1.540	0.954	−0.018	15.008	0.019	1.545	0.945	−0.014	12.820
6.000	10.13	0.029	1.497	0.915	−0.024	12.481	0.025	1.486	0.923	−0.027	15.740
8.000	10.09	0.033	1.409	0.899	−0.024	13.195	0.032	1.394	0.901	−0.021	12.294
10.000	10.06	0.042	1.350	0.875	−0.031	13.414	0.037	1.333	0.886	−0.028	13.922
15.000	10.04	0.060	1.264	0.828	−0.051	14.545	0.041	1.235	0.879	−0.034	14.729

Table 10 (EBF and EABF) G–P fitting coefficients (b, c, a, X_k and d) of ZMF4 sample

E (MeV)	Z_{eq}	EBF					EABF				
		a	b	c	d	X_k	a	b	c	d	X_K
0.015	13.97	0.261	1.023	0.350	−0.178	12.073	0.191	1.022	0.414	−0.080	11.238
0.020	14.38	0.177	1.047	0.428	−0.096	16.174	0.185	1.047	0.420	−0.103	16.078
0.030	14.83	0.213	1.147	0.394	−0.115	14.342	0.218	1.147	0.391	−0.122	13.956
0.040	15.13	0.196	1.307	0.436	−0.109	14.452	0.196	1.314	0.435	−0.109	14.672
0.050	15.34	0.167	1.501	0.509	−0.093	14.662	0.164	1.539	0.509	−0.089	15.056
0.060	17.54	0.162	1.495	0.523	−0.091	14.411	0.156	1.568	0.524	−0.086	15.381
0.080	18.01	0.111	1.736	0.655	−0.063	14.390	0.170	2.133	0.540	−0.101	13.489
0.100	18.32	0.065	1.918	0.795	−0.044	14.450	0.118	2.655	0.675	−0.082	12.863
0.150	18.85	0.009	2.162	1.010	−0.022	13.656	0.030	3.432	0.945	−0.039	13.436
0.200	19.18	−0.020	2.224	1.157	−0.015	12.036	−0.011	3.518	1.126	−0.024	12.793
0.300	19.58	−0.041	2.224	1.267	−0.011	10.215	−0.044	3.179	1.288	−0.010	9.832
0.400	19.83	−0.047	2.178	1.302	−0.009	9.615	−0.062	2.847	1.361	0.018	26.072
0.500	20.00	−0.048	2.128	1.304	−0.011	8.717	−0.067	2.615	1.380	0.012	17.030
0.600	20.10	−0.059	2.056	1.331	0.015	23.359	−0.065	2.477	1.362	0.017	20.962
0.800	20.19	−0.059	1.961	1.319	0.016	18.595	−0.064	2.259	1.342	0.015	15.928
1.000	20.21	−0.056	1.901	1.287	0.016	17.215	−0.059	2.129	1.302	0.016	16.413
1.500	14.39	−0.048	1.839	1.228	0.016	15.217	−0.050	1.942	1.238	0.018	14.626
2.000	11.31	−0.034	1.792	1.154	0.012	14.965	−0.035	1.841	1.158	0.013	14.645
3.000	10.54	−0.011	1.688	1.055	0.001	10.790	−0.009	1.707	1.050	−0.001	11.126
4.000	10.37	0.006	1.609	0.992	−0.009	14.284	0.008	1.615	0.984	−0.011	13.125
5.000	10.28	0.016	1.540	0.954	−0.019	15.035	0.019	1.545	0.945	−0.015	12.799
6.000	10.24	0.030	1.496	0.915	−0.024	12.337	0.025	1.485	0.924	−0.027	15.770
8.000	10.19	0.033	1.409	0.899	−0.024	13.234	0.033	1.394	0.901	−0.022	12.292
10.000	10.16	0.042	1.350	0.875	−0.031	13.389	0.037	1.332	0.887	−0.028	13.923
15.000	10.14	0.060	1.264	0.828	−0.052	14.524	0.041	1.234	0.881	−0.034	14.728

that the ZMF4 sample had the lowest EBF values of all the samples that were under investigation. The photon accumulation factor is referred to as the energy absorption build-up factor (EABF), and the quantity of interest is the amount of energy that is absorbed or deposited in the substance of interest. EABF values followed a trend that was comparable to that of EBF values. Tables 6–10 listed the full data of all samples at investigated photon energy range and depth. The research reveals that the incorporation of rare earth elements can significantly improve the structural and magnetic properties of ferrites. This can lead to enhanced magnetic properties, improved structural stability, controlled electrical conductivity, and customized performance for specific applications. The study also reveals that RE elements can be used to enhance magnetostrictive properties for sensors and actuators and improve magnetic permeability for antennas and magnetic recording heads. High-density data storage, transformers, and inductors can use this approach, making ferrites ideal for high-power applications. The findings also suggest that the use of RE resources can promote sustainable synthesis methods, reduce material costs, and promote the sustainable use of resources. The addition of reactive oxygen species (RE) elements to ferrite lattice sites significantly enhances their magnetic properties. This includes altering superexchange interactions, introducing anisotropy, influencing spin alignment, distorting the crystal field, and modifying the magnetic domain structure. This results in increased saturation magnetization and improved magnetic ordering. RE elements also contribute to magnetic anisotropy, resulting in higher coercivity and better stability of the magnetic domains. The pinning of magnetic domain walls also enhances coercivity and overall magnetic hardness, making RE-substituted ferrites ideal for high-performance magnetic applications.

5 Conclusions

This study successfully enhanced ZMF-spinel nanoferrite composites through Gd3+ ion doping, utilizing comprehensive analytical techniques to delve into their structural, optical, and magnetic properties. The introduction of Gd^{3+} ions notably altered lattice parameters and reduced crystallite sizes to an optimal 19.82 nm, crucially augmenting magneto-optical properties. The nanoscale dimensions were confirmed via SEM and HR-TEM, with SAED analysis corroborating XRD findings through identified diffraction rings. Significant spectral shifts in FT-IR, Raman, and XPS analyses were observed with the optimized ZMF4 sample showcasing distinct peaks and an increase in RAMAN intensity in the 1250–1750 cm^1 range as Gd^{3+} doping ratios were escalated. The research shows that adding Gd^{3+} ions to $Zn_{0.5}Mg_{0.5}Fe_2O_4$ spinel ferrites changed their structure in a big way, creating nano-sized cubic structures with a perfect crystallite size of 19.82 nm. Gd^{3+} ions, which have a net magnetic moment of 7.94 ¼B, improve the magneto-optical properties, which leads to a change in behavior that is more like a superparamagnetic one. This suggests potential applications in data storage and optical waveguides. The study also assessed the gamma-ray shielding efficiency of these materials, showing that the inclusion of Gd^{3+} ions significantly improved radiation attenuation. The optimized sample (ZMF4) displayed superior magneto-optical characteristics and outstanding gamma-ray shielding performance, especially at higher Gd^{3+} levels. When Gd^{3+} ions were added, the band gap dropped from 3.21 eV to 2.99 eV, which shows that the electronic properties were improved. Gd^{3+} is not magnetic by itself, but it changes the magnetic interactions between Fe^{3+} ions, which in turn changes the ferrite's lattice parameter, crystallinity, saturation magnetization, and coercivity. RE elements for doping face challenges like high costs, environmental impact, complex synthesis, stability issues, and health and safety risks due to their high energy consumption and high energy consumption. A notable shift in the spectral peak of O-2 1S1/2 from 529.61 eV for ZMF0 to 533.64 eV for ZMF4 underscored the impact of Gd^{3+} incorporation. Optical analyses revealed a band gap narrowing from 3.21 eV to 2.99 eV across the samples, indicative of a blue shift and enhanced electronic properties. Magnetic assessments pointed to a soft magnetic transition and identified superparamagnetic regions, emphasizing the material's potential across a wide spectrum of technological applications. FLUKA Monte Carlo simulations brought to light the nanomaterial's improved radiation shielding with increased Gd^{3+} concentration and sample thickness, showcasing a direct correlation between these factors and photon attenuation efficiency. Samples with 1 wt% Gd exhibited superior shielding, particularly noted in the significant drop in the Ln(Io/I) ratio. Increases in G_{LAC} and G_{MAC} with Gd concentration, especially across photon energies of 0.356 to 1.333 MeV, highlighted the composition's critical role in shielding effectiveness. Furthermore, the decrease in G_{HVL} with higher Gd levels underscored a denser and more effective radiation barrier. The study's findings on the exposure and energy absorption build-up factors emphasize the nuanced interplay between photon energy and material interaction, vital for advancing shielding material development. The incorporation of Gd^{3+} ions into ZMF-spinel ferrites significantly refines their structural, optical, and magnetic characteristics, while also vastly enhancing their gamma-ray shielding capabilities. These improvements suggest the material's high potential for applications in microwave devices, biomedical fields, energy systems, and notably, in radiation protection, marking a significant leap forward in the development of advanced functional composites and radiation shielding technologies.

Data availability

The data that support the findings of this study are available from the corresponding author upon reasonable request.

Acknowledgements The authors extend their appreciation to Taif University, Saudi Arabia, for supporting this work through project number (TU-DSPP-2024-44).

Author contributions Huda F. Khalil: designed the study, and coordinated the research team. Analyzed data related to structural properties. Shams A.M. Issa: Conducted experiments on magneto-optical properties. Contributed to writing and editing the manuscript. Sherif G. Elsharkawy: Performed gamma-ray shielding tests. Assisted in data interpretation. R. B. Malidarreh: Contributed to the synthesis and doping process of ZMF-Spinel Ferrites. Sara Gad: Involved in material characterization and data analysis. Participated in manuscript preparation. Ali Badawi: Writing – review & editing, Project administration. Fatma Fakhry: Assisted in the experimental design and performed statistical analysis. Contributed to drafting the manuscript. Hesham M.H. Zakaly: Led the project, Oversaw the entire research process, provided critical revisions of the manuscript, and contributed to the discussion of results.

Funding This research was funded by Taif University, Saudi Arabia, Project No. (TU-DSPP-2024-44).

Compliance with ethical standards

Conflict of interest The authors declare that no competing interests.

References

1. Asghar HMNHK, Hussain M, Aslam S et al. (2021) Tuning the dielectric and structural properties of erbium substitution on cobalt ferrites. J Ovonic Res 17:383–394
2. Vinod G, Rajashekhar K, Ravinder D, Naik JL (2021) Structural, electrical, and magnetic properties of erbium (Er3+) substituted Cu–Cd nano-ferrites. J Mater Sci Mater Electron 32:24069–24082. https://doi.org/10.1007/S10854-021-06869-4
3. Gilani ZA, Farooq A, Noor HM et al. (2020) Synthesis and Characterization of Lanthanum doped Co-Zn Spinel Ferrites Nanoparticles by Sol-Gel Auto Combustion Method. J Mater Phys Sci 1:1–11. https://doi.org/10.52131/JMPS.2020.0101.0001
4. Aslam A, Rehman A, Amin N, et al. (2021) Lanthanum doped Zn0.5Co0.5LaxFe2− xO4 spinel ferrites synthesized via co-precipitation route to evaluate structural, vibrational, electrical, optical, dielectric, and thermoelectric properties. J Phys Chem Solids. https://doi.org/10.1016/j.jpcs.2021.110080
5. Aslam A, Razzaq A, Naz S et al. (2021) Impact of Lanthanum-Doping on the Physical and Electrical Properties of Cobalt Ferrites. J Supercond Nov Magn 34:1855–1864. https://doi.org/10.1007/S10948-021-05802-4
6. Raza W, Nabi G, Shahzad A et al. (2021) Electrochemical performance of lanthanum cerium ferrite nanoparticles for supercapacitor applications. J Mater Sci Mater Electron 32:7443–7454. https://doi.org/10.1007/S10854-021-05457-W
7. Roman T, Ghercă D, Borhan AI et al. (2021) Nanostructured quaternary Ni1-xCuxFe2-yCeyO4 complex system: Cerium content and copper substitution dependence of cation distribution and magnetic-electric properties in spinel ferrites. Ceram Int 47:18177–18187. https://doi.org/10.1016/J.CERAMINT.2021.03.136
8. Meena S, Anantharaju KS, Vidya YS et al. (2021) Enhanced sunlight driven photocatalytic activity and electrochemical sensing properties of Ce-doped MnFe2O4 nano magnetic ferrites. Ceram Int 47:14760–14774. https://doi.org/10.1016/J.CERAMINT.2020.11.105
9. Andrade RGD, Veloso SRS, Castanheira EMS (2020) Shape anisotropic iron oxide-based magnetic nanoparticles: Synthesis and biomedical applications. International J Mol Sci. https://doi.org/10.3390/ijms21072455
10. Hussain K, Amin N, Arshad MI (2021) Evaluation of structural, optical, dielectric, electrical, and magnetic properties of Ce3+ doped Cu0.5Cd0.25Co0.25Fe2-xO4 spinel nano-ferrites. Ceramics Int 47:3401–3410. https://doi.org/10.1016/j.ceramint.2020.09.185
11. Kefeni KK, Msagati TAM, Mamba BB (2017) Ferrite nanoparticles: Synthesis, characterisation and applications in electronic device Mater Sci Eng B 215:37–55. https://doi.org/10.1016/J.MSEB.2016.11.002
12. Ranga R, Kumar A, Kumari P et al. (2021) Ferrite application as an electrochemical sensor: A review. Mater Charact 178:111269. https://doi.org/10.1016/J.MATCHAR.2021.111269
13. Qindeel R, Alonizan NH, Alghamdi EA, Awad MA (2021) Synthesis and characterization of spinel ferrites for microwave devices. J Sol Gel Sci Technol 97:593–599. https://doi.org/10.1007/s10971-021-05470-9
14. Shakil M, Inayat U, Arshad M, et al. (2020) Influence of zinc and cadmium co-doping on optical and magnetic properties of cobalt ferrites. Ceramics Int 46:7767–7773
15. Margabandhu M, Sendhilnathan S, Senthilkumar S, Gajalakshmi D (1610) Investigation of structural, morphological, magnetic properties and biomedical applications of Cu2+ substituted uncoated cobalt ferrite nanoparticles. Braz Arch Biol Technol 59:16161046. https://doi.org/10.1590/1678-4324-2016161046
16. Selima S, Khairy M, Mousa MA (2019) Comparative studies on the impact of synthesis methods on structural, optical, magnetic and catalytic properties of CuFe2O4. Ceramics Int 45:6535–6540
17. Priya A, Geetha D, Kavitha N (2019) Effect of Al substitution on the structural, electric and impedance behavior of cobalt ferrite. Vacuum 160:453–460
18. Anupama M, Rudraswamy B, Dhananjaya A (2017) Investigation on impedance response and dielectric relaxation of Ni-Zn ferrites prepared by self-combustion technique. Journal Alloy Compd 706:554–561
19. Loan NTT, Lan NTH, Hang NTT, et al. (2019) CoFe2O4 Nanomaterials: Effect of Annealing Temperature on Characterization, Magnetic, Photocatalytic, and Photo-Fenton Properties. Processes. https://doi.org/10.3390/pr7120885
20. Masunga N, Mmelesi O, (2019) Recent advances in copper ferrite nanoparticles and nanocomposites synthesis, magnetic properties and application in water treatment. J Environ Chem Eng 7:103179
21. Sundararajan M, Sailaja V, Kennedy L, et al. (2017) Photocatalytic degradation of rhodamine B under visible light using nanostructured zinc doped cobalt ferrite: kinetics and mechanism. Ceramics Int 43:540–548
22. Kefeni K, Mamba B, Msagati TAM (2017) Application of spinel ferrite nanoparticles in water and wastewater treatment: a review. Separation Purif Technol 188:399–422
23. Chand P, Vaish S, Kumar P (2017) Structural, optical and dielectric properties of transition metal (MFe2O4; M= Co, Ni and Zn) nanoferrites. Physica B: Condensed Matter 524:53–63
24. Ali AM, Issa SAM, Algarni H et al. (2021) Structural, surface morphology and radiation shielding properties of barium ferrite powder. Phys Scr 96. https://doi.org/10.1088/1402-4896/ac03e0

25. Zakaly HMH, Issa SAM, Saudi HA, et al. (2022) Structure, Mössbauer, electrical, and γ-ray attenuation-properties of magnesium zinc ferrite synthesized co-precipitation method. Sci Rep 12. https://doi.org/10.1038/S41598-022-17311-Y
26. Hussein MM, Saafan SA, Abosheiasha HF et al. (2023) Impact of the Ni/Co ratio on structural and magnetic properties in A-site stoichiometric nanosized spinel ferrites. Ceram Int 49:39107–39116. https://doi.org/10.1016/j.ceramint.2023.09.250
27. Henaish AMA, Mostafa M, Salem BI et al. (2020) Spectral, electrical, magnetic and radiation shielding studies of Mg-doped Ni–Cu–Zn nanoferrites. J Mater Sci Mater Electron **3122**(31):20210–20222. https://doi.org/10.1007/S10854-020-04541-X
28. Mostafa AMA, Elbashir BO, Issa SAM et al. (2022) Influence of combining Al2O3, La2O3, Gd2O3, and Dy2O3with barium borosilicate glass-ceramics: A case study of gamma radiation interaction parameters. J Mater Res Technol 19:1972–1981. https://doi.org/10.1016/j.jmrt.2022.05.095
29. Duong GV, Sato Turtelli R, Thuan BD et al. (2007) Magnetic properties of nanocrystalline BaFe12O19 prepared by hydrothermal method. J Non Cryst Solids 353:811–813. https://doi.org/10.1016/J.JNONCRYSOL.2006.12.047
30. Morrish AH (2001) The physical principles of magnetism. The Physical Principles of Magnetism. 1–700 p. https://doi.org/10.1109/9780470546581
31. Zhang Y, Yang Y, Dong Z et al. (2020) Enhanced photocatalytic activity of Ba doped BiFeO3 by turning morphologies and band gap. J Mater Sci Mater Electron 31:15007–15012. https://doi.org/10.1007/S10854-020-04064-5
32. Ayyar M, Hema E, Manikandan A et al. (2016) The role of Mn2+-doping on structural, morphological, optical, magnetic and catalytic properties of spinel ZnFe2O4 nanoparticles. ingentaconnect.comE Hema, A Manikandan, M Gayathri, M Durka, SA Antony, BR Venkatraman. J Nanosci Nanotechnol, 2016 15:1–15. https://doi.org/10.1166/jnn.2016.11037
33. Revathi J, Abel M, Archana V, et al. Synthesis and characterization of CoFe2O4 and Ni-doped CoFe2O4 nanoparticles by chemical Co-precipitation technique for photo-degradation of organic dyestuffs. Phys B Condensed Matter 587:412136
34. Cai C, Liu J, Zhang Z, et al. (2016) Visible light enhanced heterogeneous photo-degradation of Orange II by zinc ferrite (ZnFe2O4) catalyst with the assistance of persulfate. Separation Purif Technol 165:42–52
35. Renukadevi S, Jeyakumari AP (2020) Rational design of ZnFe2O4/g-C3N4 heterostructures composites for high efficient visible-light photocatalysis for degradation of aqueous organic pollutants. Inorganic Chem Commun 118:108047
36. Zhang X, Lin B, Li X et al. (2022) MOF-derived magnetically recoverable Z-scheme ZnFe2O4/Fe2O3 perforated nanotube for efficient photocatalytic ciprofloxacin removal. Chem Eng J 430:132728. https://doi.org/10.1016/J.CEJ.2021.132728
37. Riaz K, Nadeem S, Chrouda A, et al. Coupling of Se-ZnFe2O4 with rGO for spatially charged separated nanocomposites as an efficient photocatalyst for degradation of organic pollutants in natural. Colloids Surfaces A Physicochem Eng Asp 649:129332
38. Miao Z, Tao J, Li S, et al. Popcorn-like ZnFe2O4/CdS nanospheres for high-efficient photocatalyst degradation of rhodamine B. Colloids Surfaces A Physicochem Eng Asp 654:130127
39. Medeiros PN, Gomes YF, Bomio MRD et al. (2015) Influence of variables on the synthesis of CoFe2O4 pigment by the complex polymerization method. J Adv Ceram 135–141. https://doi.org/10.1007/s40145-015-0145-1
40. Nechvílová K, Kalendová A (2015) Properties of organic coatings containing pigments with surface modified with a layer of ZnFe2O4. Adv Sci Technol Res J, 9:51–55
41. Ewunkem AJ, Rodgers L, Campbell D et al. (2021) Experimental Evolution of Magnetite Nanoparticle Resistance in Escherichia coli. Nanomaterials 11:790. https://doi.org/10.3390/nano11030790
42. Ashour A, El-Batal A, Maksoud M, et al. Antimicrobial activity of metal-substituted cobalt ferrite nanoparticles synthesized by sol–gel technique. Particuology 40:141–151
43. Suleman M, Riaz S (2020) In silico study of hyperthermia treatment of liver cancer using core-shell CoFe2O4@ MnFe2O4 magnetic nanoparticles. J Magn Magn Mater 498:166143
44. Dippong T, Andrea Levei E, Cadar O, De Julian Fernandez C (2021) Recent Advances in Synthesis and Applications of MFe2O4 (M = Co, Cu, Mn, Ni, Zn) Nanoparticles. Nanomaterials. https://doi.org/10.3390/nano11061560
45. Slimani Y, Almessiere M, Korkmaz A, et al. (2019) Ni0.4Cu0.2Zn0.4TbxFe2-xO4 nanospinel ferrites: ultrasonic synthesis and physical properties. Ultrasonics Sonochemistry 59:104757
46. Ilosvai AM, Dojcsak D, Váradi C, et al. (2022) Sonochemical combined synthesis of nickel ferrite and cobalt ferrite magnetic nanoparticles and their application in glycan. International J Mol Sci, https://doi.org/10.3390/ijms23095081
47. Fuentes-García A, Alavarse AC, Maldonado ACM et al. (2020) Simple sonochemical method to optimize the heating efficiency of magnetic nanoparticles for magnetic fluid hyperthermia. ACS Omega. 2020:5:26357–26364, https://doi.org/10.1021/acsomega.0c02212.
48. Bang J, Suslick KS (1990) Applications of ultrasound to the synthesis of nanostructured materials. Adv Mater. 22:1039–1059. https://doi.org/10.1002/adma.200904093
49. Yadav R, Kuřitka I, Vilcakova J, et al. Impact of sonochemical synthesis condition on the structural and physical properties of MnFe2O4 spinel ferrite nanoparticles. ElsevierRS Yadav, I Kuřitka, J Vilcakova, T Jamatia, M Machovsky, D Skoda, P Urbánek, M MasařUltrasonics sonochemistry, 2020•Elsevier
50. Yousefi S, Amiri O, sonochemistry MS-N-U, 2019 undefined Control sonochemical parameter to prepare pure Zn0. 35Fe2. 65O4 nanostructures and study their photocatalytic activity. ElsevierSR Yousefi, O Amiri, M Salavati-NiasariUltrasonics sonochemistry, 2019•Elsevier
51. Sertkol M, Slimani Y, Almessiere M, et al. Sonochemical synthesis of Mn0. 5Zn0. 5ErxDyxFe2-2xO4 (x≤ 0.1) spinel nanoferrites: magnetic and textural investigation. Elsevier
52. Tsuji M (2022) Microw ave-assisted synthesis of metallic nanomaterials in liquid phase. Chemistry Select. 2:805–819. https://doi.org/10.1002/slct.201700011
53. Zhu YJ, Chen F (2014) Microwave-assisted preparation of inorganic nanostructures in liquid phase. Chem Rev. 114:6462–6555. https://doi.org/10.1021/CR400366S
54. Maksoud M, Sami N, Hassan H, et al. (2022) Novel adsorbent based on carbon-modified zirconia/spinel ferrite nanostructures: Evaluation for the removal of cobalt and europium radionuclides from aqueous. J Colloid Interface Sci 607:111–124
55. Magdalane C, Priyadharsini G, Kaviyarasu K, Irudaya Jothi A, Gnanamani Simiyon G (2021) Synthesis and characterization of TiO2 doped cobalt ferrite nanoparticles via microwave method: Investigation of photocatalytic performance of congo red degradation. Surfaces Interfaces 25:101296
56. Naik MM, Naik HSB, Kottam N et al. (2019) Multifunctional properties of microwave-assisted bioengineered nickel doped cobalt ferrite nanoparticles. J Sol Gel Sci Technol 91:578–595. https://doi.org/10.1007/s10971-019-05048-6
57. Kalia S, Kumar A, Munjal N, Prasad N, (2021) Synthesis of ferrites using various parts of plants: a mini review. J Phys Conf Ser 1964:32003. https://doi.org/10.1088/1742-6596/1964/3/032003
58. Thakur P, Taneja S, Chahar D, et al. (2021) Recent advances on synthesis, characterization and high frequency applications of Ni-Zn ferrite nanoparticles. Journal Magn Magn Mater 530:167925

59. Yew Y, Shameli K, Miyake M, et al. (2020) Green biosynthesis of superparamagnetic magnetite Fe3O4 nanoparticles and biomedical applications in targeted anticancer drug delivery system: A review. J Chem 20:2287–2308
60. Wani TA, Suresh G (2022) Plant-Mediated Green Synthesis of Magnetic Spinel Ferrite Nanoparticles: A Sustainable Trend in Nanotechnology. Adv Sustain Syst 6. https://doi.org/10.1002/ADSU.202200035
61. Bharde AA, Parikh RY, Baidakova M et al. (2008) Bacteria-mediated precursor-dependent biosynthesis of superparamagnetic iron oxide and iron sulfide nanoparticles. Langmuir 24:5787–5794. https://doi.org/10.1021/LA704019P
62. Chutia R, Chetiya B (2018) Biogenic CuFe2O4 magnetic nanoparticles as a green, reusable and excellent nanocatalyst for acetylation reactions under solvent-free conditions. New J Chem 42:15200–15206
63. Karunakaran G, Jagathambal M, Van Minh N et al. (2018) Green Synthesis of NiFe2O4 Spinel-Structured Nanoparticles Using Hydrangea paniculata Flower Extract with Excellent Magnetic Property. JOM 70:1337–1343. https://doi.org/10.1007/S11837-018-2871-7
64. Perez-Gonzalez T, Jimenez-Lopez C, Neal AL et al. (2010) Magnetite biomineralization induced by Shewanella oneidensis. Geochim Cosmochim Acta 74:967–979. https://doi.org/10.1016/J.GCA.2009.10.035
65. Zhou W, He W, Zhong S et al. (2009) Biosynthesis and magnetic properties of mesoporous Fe3O4 composites. J Magn Magn Mater 321:1025–1028. https://doi.org/10.1016/J.JMMM.2008.10.007
66. Zhou W, He W, Zhang X et al. (2009) Biosynthesis of iron phosphate nanopowders. Powder Technol 194:106–108. https://doi.org/10.1016/J.POWTEC.2009.03.034
67. Bose S, Hochella MF, Gorby YA, et al. (2009) Bioreduction of hematite nanoparticles by the dissimilatory iron reducing bacterium Shewanella oneidensis MR-1. Cosmochim Acta, https://doi.org/10.1016/j.gca.2008.11.031
68. Sodaee T, Ghasemi A, Razavi RS, (2017) Cation distribution and microwave absorptive behavior of gadolinium substituted cobalt ferrite ceramics. Journal Alloy Compd 706:133–146
69. Kardile HJ, Somvanshi SB, Chavan AR et al. (2020) Effect of Cd2+ doping on structural, morphological, optical, magnetic and wettability properties of nickel ferrite thin films. Optik 207:164462. https://doi.org/10.1016/J.IJLEO.2020.164462
70. Amri N, Massoudi J, Nouri K, et al. (2021) Influence of neodymium substitution on structural, magnetic and spectroscopic properties of Ni–Zn–Al nano-ferrites. RSC Adv, https://doi.org/10.1039/d0ra10140k
71. John S, Prakash P, Nair AM, et al. Magnetic properties of copper doped nickel ferrite nanoparticles synthesized by Co precipitation method. IOP Conf Ser Mater Sci Eng, https://doi.org/10.1088/1757-899X/310/1/012024
72. Ahmad M, Khan M, Mahmood A et al. (2018) Role of ytterbium on structural and magnetic properties of NiCr0. 1Fe1. 9O4 co-precipitated ferrites. Ceramics Int 44:5433–5439
73. Soufi A, Hajjaoui H, Elmoubarki R, Abdennouri M, Qourzal S, Barka N (2021) Spinel ferrites nanoparticles: Synthesis methods and application in heterogeneous Fenton oxidation of organic pollutants–A review. Applied Surf Sci Adv 6:100145
74. Routray KL, Saha S, Behera D (2019) Rare-earth (La3+) substitution induced changes in the structural, dielectric and magnetic properties of nano-CoFe2O4 for high-frequency and magneto-recording devices. Appl Phys A Mater Sci Process 125:1–15. https://doi.org/10.1007/s00339-019-2615-8
75. Narang SB, Pubby K (2021) Nickel spinel ferrites: a review. J Magn Magn Mater 519:167163
76. Routray KL, Saha S, Behera D (2019) DC Electrical Resistivity, Dielectric, and Magnetic Studies of Rare-Earth (Ho3+) Substituted Nano-Sized CoFe2O4. Phys Status Solidi Basic Res 256:1800676. https://doi.org/10.1002/pssb.201800676
77. Elazaka AI, Zakaly HMH, Issa SAM et al. (2021) New approach to removal of hazardous Bypass Cement Dust (BCD) from the environment: 20Na2O-20BaCl2-(60-x)B2O3-(x)BCD glass system and Optical, mechanical, structural and nuclear radiation shielding competences. J Hazard Mater 403:123738. https://doi.org/10.1016/j.jhazmat.2020.123738
78. Almousa N, Issa SAM, Tekin HO, et al. (2024) Enhancing radiation shielding transmission factors and mechanical Robustness of borosilicate glasses through Bi2O3 modification: A comprehensive study. Radiat Phys Chem 220. https://doi.org/10.1016/j.radphyschem.2024.111683
79. Battistoni G, Cerutti F, Fassò A, et al. (2007) The FLUKA code: Description and benchmarking. AIP Conf Proc 896:31–49. https://doi.org/10.1063/1.2720455
80. Malidarreh RB, Akkurt I, Almousa N, Zakaly HMH (2024) Exploring the impact of sulfur-antimony incorporation on the radiation shielding, structural, physical, and electrical properties of (S3Sb2)x(S2Ge)100−x chalcogenide composites. Opt Quantum Electron 56:195–207. https://doi.org/10.1007/s11082-024-06381-z
81. Issa SAM, Abulyazied DE, Alrowaily AW et al. (2023) Improving electrical, optical and radiation shielding properties of polyvinyl alcohol yttrium oxide composites. J Rare Earths 41:2002–2009. https://doi.org/10.1016/j.jre.2023.02.013
82. Zakaly HMH, Saudi HA, Tekin HO et al. (2021) Glass fabrication using ceramic and porcelain recycled waste and lithium niobate: physical, structural, optical and nuclear radiation attenuation properties. J Mater Res Technol 15:4074–4085. https://doi.org/10.1016/J.JMRT.2021.09.138
83. Zakaly HMH, Rashad M, Tekin HO et al. (2021) Synthesis, optical, structural and physical properties of newly developed dolomite reinforced borate glasses for nuclear radiation shielding utilizations: An experimental and simulation study. Opt Mater 114:110942. https://doi.org/10.1016/j.optmat.2021.110942
84. Ali AM, Issa SAM, Zakaly HMH et al. (2020) Structural and shielding properties of NiO/xCo3O4 nanocomposites synthesized by microwave irradiation method. Results Phys 19:103488. https://doi.org/10.1016/j.rinp.2020.103488
85. Başgöz Ö, Güler SH, Güler Ö, et al. (2022) Synergistic effect of boron nitride and graphene nanosheets on behavioural attitudes of polyester matrix: Synthesis, experimental and Monte Carlo simulation studies. Diam Relat Mater 126. https://doi.org/10.1016/j.diamond.2022.109095
86. Singh VP, Badiger NM (2014) Energy absorption buildup factors, exposure buildup factors and Kerma for optically stimulated luminescence materials and their tissue equivalence for radiation dosimetry. Radiat Phys Chem 104:61–67. https://doi.org/10.1016/j.radphyschem.2013.11.025